Optical control of 4*f* orbital state in rare-earth metals

N. Thielemann-Kühn[1], T. Amrhein[1], W. Bronsch[1], S. Jana[2], N. Pontius[2], R. Y. Engel[3], P. S. Miedema[3], D. Legut[4], K. Carva[5], U. Atxitia[1], B. E. van Kuiken[6], M. Teichmann[6], R. E. Carley[6], L. Mercadier[6], A. Yaroslavtsev[6,7], G. Mercurio[6], L. Le Guyader[6], N. Agarwal[6], R. Gort[6], A. Scherz[6], M. Beye[3], P. M. Oppeneer[7], M. Weinelt[1] and C. Schüßler-Langeheine[2]

[1]Freie Universität Berlin, Fachbereich Physik, Arnimallee 14, 14195 Berlin, Germany
[2]Helmholtz-Zentrum Berlin für Materialien und Energie GmbH, Albert-Einstein-Str. 15, 12489 Berlin, Germany
[3]Deutsches Elektronen-Synchrotron DESY, Notkestr. 85, 22607 Hamburg, Germany
[4]IT4Innovations-Czech National Supercomputing Centre, VSB - Technical University Ostrava, 17. listopadu 2172/15, 708 00 Ostrava, Czech Republic
[5]Charles University, Faculty of Mathematics and Physics, DCMP, Ke Karlovu 5, 12116 Prague 2, Czech Republic
[6]European XFEL, Holzkoppel 4, 22869 Schenefeld, Germany
[7]Uppsala University, Department of Physics and Astronomy, P.O. Box 516, 75120 Uppsala, Sweden

Information technology demands continuous increase of data-storage density.[1] In high-density magnetic recording media, the large magneto-crystalline anisotropy (MCA) stabilizes the stored information against decay through thermal fluctuations. In the latest generation storage media, MCA is so large that magnetic order needs to be transiently destroyed by heat to enable bit writing[2]. Here we show an alternative approach to control high-anisotropy magnets: With ultrashort laser pulses the anisotropy itself can be manipulated via electronic state excitations. In rare-earth materials like terbium metal, magnetic moment and high MCA both originate from the 4*f* electronic state[3]. Following infrared laser excitation 5*d*-4*f* electron-electron scattering processes lead to selective orbital excitations that change the 4*f* orbital occupation and significantly alter the MCA. Besides these excitations within the 4*f* multiplet, 5d-4*f* electron transfer causes a transient change of the 4*f* occupation number, which, too, strongly alters the MCA. Such MCA change cannot be achieved by heating: The material would rather be damaged than the 4*f* configuration modified[4]. Our results show a way to overcome this limitation for a new type of efficient magnetic storage medium. Besides potential technological relevance, the observation of MCA-changing excitations also has implications for a general understanding of magnetic dynamics processes on ultrashort time scales, where the 4*f* electronic state affects the angular momentum transfer between spin system and lattice[5].

Introduction

Optical control of magnetism bears the potential for novel data information technologies with faster processing time and lower energy consumption[6-8]. A technological challenge is the control of particular properties of the spin system by, e.g., locally changing the spin-spin coupling or the interaction of spins and their environment[9]. The latter occurs via spin-orbit coupling (SOC), linking the spin system with the crystal-electric field of the surrounding ions. Strong SOC is the basis for magneto-crystalline anisotropy (MCA) which stabilizes spin orientations in certain crystalline directions. The MCA-related energy barrier preventing spin rotation is a key ingredient for high-density magnetic storage as it stabilizes the spins in small magnetic units against thermal fluctuations. A condition for strong MCA is an orbital ground state with anisotropic charge distribution that itself is stable against thermal excitations. In turn, controlling the orbital state could provide a handle to manipulate MCA[10].

Large SOC is a property of heavy elements, which are essential in every high-MCA material. In this context the rare earth elements are particularly interesting. Their strongly localized 4*f* electrons carry large magnetic moments and strong SOC stabilizes their Hund's rule orbital ground state[11]. How dramatically the orbital state affects MCA can be seen from a comparison of the two neighboring rare earth elements gadolinium (Gd) and terbium (Tb). Both are Heisenberg-like ferromagnets with similar crystalline and valence band structure, but Gd with $4f^7$ configuration shows negligible MCA while that of Tb with $4f^8$ configuration is exceptionally high. In Gd the half-filled 4*f* shell with all (majority) spins parallel has a spherical charge distribution and MCA energy per atom of only 0.03 meV[11]. Tb has one additional electron of opposite (minority) spin orientation in the state with magnetic quantum number $m_\ell = 3$. This changes the charge distribution to strongly anisotropic such that Tb metal has the highest MCA energy among the 4*f* elements of 12 meV per atom[12].

The energy needed to change the orbital state in Tb is even larger than the MCA energy. Placing the minority electron into the first excited $m_\ell = 2$ state requires an energy of 280 meV (Table S2, Supplementary Information, SI), i.e., more than 3000 K. A change of the 4*f* occupation number via transfer of an electron to or from the 5*d* states requires energies of 2.3 and 2.7 eV, respectively. Hence, in thermal equilibrium any considerable change of orbital state of Tb (or another high anisotropy heavy element) requires temperatures that would destroy a magnetic solid-state device – a fact reflecting the high MCA[4].

The situation is different, though, when the system is brought out of equilibrium. Optical laser pulses initially only heat the electron system. Even for moderate laser power well below any damage threshold, the electron system transiently reaches temperatures of several thousands of Kelvin[13]. Optical pumping does not drive excitations within the 4*f* system directly but, as we show in the following, they occur via inelastic scattering with laser-excited valence electrons. We detect these 4*f* excitations with time-resolved X-ray

absorption spectroscopy (XAS) utilizing that the spectral shape directly reflects the 4*f* orbital state (Methods & Fig. S4, SI).

Experimental Results

As depicted by the experimental scheme in Fig. 1a, we recorded X-ray absorption spectra by probing the transmission through a thin Tb film deposited on a silicon nitride membrane. We excited our sample with 800 nm laser pulses and probed with monochromatic X-ray pulses from EuXFEL at a delay of 150 fs. Figure 1b shows spectra recorded in this way. The M_5 resonance is a transition into a partially occupied 4*f* state, which leaves behind a $3d_{5/2}$ core-hole with spin- and orbital moment aligned. The blue dots reflect the Tb M_5 absorption multiplet with 4*f* electrons in the $^7F_6$ ground state ("unpumped"). The second spectrum (orange dots, "pumped") was recorded 150 fs after exciting the sample by the pump-laser pulse. The difference in the spectral shape (Fig. 1c) indicates that pumping has changed the 4*f* electronic state. (We verified this with a reference experiment on Gd, see SI, Fig. S1)

The pump-induced change of absorption shows a characteristic temporal evolution. In Fig. 1d we present the differential X-ray absorption at 1236 eV versus the delay between the IR-pump and X-ray probe pulses (black data points). The absorption at this energy drops rapidly within 100 fs, reaches a maximum deviation from the ground state of -3 % after 200 fs and recovers with a time constant of 1.3 ps. These time scales resemble those for optically excited valence electrons in metals[13,14].

The pumped spectra change with delay. Figure 2a presents an energy vs. delay map illustrating the differential absorption for the first 430 fs after pumping. Difference spectra (Fig. 2b) averaged over two successive delay ranges (I) and (II) (marked in Fig. 2a by white vertical separation lines and color-coded in Fig. 1c) show that the dip at 1235.8 eV becomes more pronounced with time while the one at 1237.5 eV changes only slightly, and for energies around 1235 eV we find the absorption to increase (see SI, Fig. S2 for error bars). Obviously the 4*f* state evolves in time.

Excitation channels

Optical excitations of electrons require a change of orbital quantum number, so, direct optical excitations within the 4*f* multiplet are not allowed. Excitations from the itinerant 5*d* valence states into the localized 4*f* states or vice versa require energies of 2.8 and 2.3 eV, respectively[15] exceeding the 1.55 eV of the pump laser photons. (Two-photon absorption processes are negligible under our experimental conditions, see Section 11, SI). The pump laser hence cannot alter the 4*f* state directly, but excites the valence electrons of mixed 5*d* and 6*s* character. Directly after absorption of an ideally short pulse, the valence-band electron-energy distribution can be described by the grey rectangles in Fig. 3a: A part of the electrons is excited to previously empty states above the Fermi energy E_F, leaving behind holes below E_F. The pump photon energy

defines the energy scale for electron-hole pair excitations to $E_F \pm 1.55$ eV. By inelastic Coulomb scattering, these optically excited 5*d* electrons can transfer energy and angular momentum to the 4*f* system (Fig. 3a, bottom panel). Scattering in the electron system eventually leads to a hot Fermi distribution of the valence electrons with an electron temperature T_e of above 4000 K for our experiment (see Fig. 1c and SI, Fig. S3). This electron energy distribution extends beyond the initial pump energy such that electrons at 2.8 eV above the Fermi energy can reach an empty 4*f* state and holes 2.3 eV below E_F can accept the most lightly bound minority spin electron of Tb as depicted in Fig. 3b.

We can expect this channel to be efficient: 4*f*-5*d* electron-transfer is related to the overlap and thus hybridization of 5*d* and 4*f* states, which is the foundation of the RKKY exchange interaction (Ruderman–Kittel–Kasuya–Yosida)[3], mediating the magnetic order in rare earth metals. The strong 5*d*-4*f* intra-atomic exchange suggests this hybridization to be strong.

Spectral changes

Even within our best temporal resolution of 65 fs, we cannot observe the short-living non-equilibrium electronic state of Fig. 3a. We rather expect contributions from both 5*d*-4*f*-scattering and electron transfer for all delays but with varying relative weight.

We start by analyzing the spectral changes 150 fs after the pump presented in Figs. 1b and c. For that, we describe the 4*f* ground and excited state spectra with atomic multiplet calculations (see SI, Fig. S4)[16]. We find the description of the unpumped spectrum most accurate in the energy region of the two prominent peaks[17] (see SI, Fig. S5). We therefore concentrate on this energy range for the analysis. The lowest-energy excitation of the minority electron from $m_\ell = 3$ to $m_\ell = 2$ leads to the $^7F_5$ state. An admixture of about 16 % $^7F_5$ indeed qualitatively describes the overall shape of the differential absorption at 150 fs delay (see SI, Fig. S6), but the quantitative disagreement of the spectra suggests additional contributions from other excitations. Including higher $4f^8$ excited states (m_ℓ = 1, 0, -1, -2, -3) with either a Boltzmann or Fermi distribution for their relative population improves the description somewhat (see SI, Fig. S7 and S8), but the relative weight of these higher excited states is much lower than to be expected. Expressed in electron temperatures we obtain around 1500 K for the 4*f* system, which is far below the 4000 K valence electron temperature (c.f. blue curve in Fig. 1c). This, together with the overall poor agreement between this simulation and experimental data, implies that a 4*f*-5*d* thermalization does not involve higher excited 4*f* states.

A much better quantitative description is obtained by including $4f^9$ and $4f^7$ multiplets in our calculation instead. The best fit (orange and black solid lines in Fig. 1b) contains 20 % of the $^7F_5$ excited $4f^8$ state, and 4 % of $4f^9$ and 3 % of $4f^7$ electron-transfer contributions. We note that the dominant $^7F_5$ contribution leads to a transfer of spectral weight from the M_5 to the M_4 resonance, which is what we indeed observe (see SI, Fig. S9). Including $4f^7$ and $4f^9$ multiplets in the description requires some assumptions. The spectral shape

itself can readily be simulated (and experimentally observed in Gd and Dy, respectively). Unlike for the orbital-excited $4f^8$ states, our atomic multiplet calculation does not provide the energy position of the $4f^7$ and $4f^9$ multiplets relative to $4f^8$. It depends critically on core-hole screening, which is altered by adding or removing a localized 4*f* electron. We addressed this by estimating the relative energy positions from the energy separation between the $^7F_5$, $^7F_4$, and $^7F_3$ multiplet terms (see SI, Tab. S2). We then determined the effect on the core-hole screening by optimizing the energy shift to match the experimental data (see SI for details).

We find our description of $4f^7$ and $4f^9$ contributions supported by the spectral changes on short delay scales presented in Fig. 2a and b. As these states become populated only after the 5*d* electron system has thermalized, we expect lower contributions for short delays. In fact, we can readily describe spectral changes in Fig. 2b by different $4f^7$ and $4f^9$ contributions (solid lines in Fig. 2b). The $4f^9$ weight grows from 1.9 % in interval (I) to 4.6 % in interval (II), for $4f^7$ it is from 1.9 % to 2.8 %. Surprisingly, the contribution of the $4f^9$ increases more than that of the $4f^7$. We speculate that this may be related to the different 5*d* density of states below and above E_F, affecting the 5*d*-4*f* hybridization[18]. As there is still no way to describe both the 4*f* and 5*d* electronic structure of rare earth metals in the same model, a quantitative description of *d-f* scattering and electron transfer is currently beyond the state-of-the-art.

The excitation mechanism via inelastic 5*d*-4*f* scattering is also reflected in the recovery behaviour of the differential absorption signal (black symbols in Fig. 1d). We find it to recover faster than the 5*d* electron temperature derived from a two-temperature model (blue line in Fig. 1d, for details see Section 3, SI). This matches the fact that only 5*d* electrons with energies above a threshold cause 4*f* excitations; excited electrons at lower energies do not contribute to the spectral change. Considering only the strongest $^7F_5$ excitation at 280 meV and assuming for simplicity a constant density of states, the 5*d* electron temperature gives an accurate prediction for the recovery of 4*f* excitations (black line in Fig. 1c).

The absence of $4f^8$ excitations with $\Delta J \neq -1$ further reveals details of the excitation mechanism. We assign it to inelastic spin-flip scattering via screened Coulomb interaction between 5*d* and 4*f* electrons changing the 5*d* spin by $\Delta S = 1$ (Fig. 3a). As one might expect, multiple higher-order scattering processes allowing for larger angular momentum transfer are negligible. A simple estimate shows that we transfer about 9 % of the absorbed laser energy into the 4*f* system (see SI, Section 10).

Transient orbital momentum change

Excitations of the 4*f* system change its orbital momentum (see Fig. 3). With total angular momentum $J = L + S$ conserved, such a change of *L* requires angular momentum transfer between the 5*d* and 4*f* electronic system. Thus our observation may help to understand the angular momentum flow in non-equilibrium magnetization dynamics of Tb and other rare earth ions[19]. This is particularly true since the direct coupling between 4*f*

system and the laser excited lattice has been identified as an important channel in magnetic dynamics of rare earth metals[5,20]. As 4*f*-state excitations will strongly affect this coupling, they need to be taken into account for a full description of the process.

MCA change

We set out to manipulate MCA via optical pulses and we now verify that we reached this goal. We determined the MCA for the Tb m_ℓ = 3 ground state and the m_ℓ = 2 excited state from all-electron first-principles calculations (see Methods). For the ground state our *ab initio* calculations provide an MCA of 15 meV per atom with a preferential orientation of magnetic moments (easy axis) in the hcp basal plane along the crystallographic *a* axis, both of which are consistent with experiment[12]. When we modify the minority Tb 4*f* electron occupation to the m_ℓ = 2 state and perform a one-step calculation of the total energies, we find the easy axis to rotate: A magnetization along the *c* axis perpendicular to the basal plane becomes preferred. The reorientation of the easy axis from in-plane to out-of-plane corresponds to an MCA sign change. We further verified this result by creating a self-consistent state with dominant m_ℓ = 2 occupation by modifying the Coulomb repulsion between the 4*f* electrons (adjustment of Hubbard U), which, too, causes the MCA sign to change.

Our results show that in Tb metal a control of the m_ℓ state within the $4f^8$ multiplet indeed strongly alters MCA. The same is true for excitations that modify the 4*f* occupation. In particular removing one electron from the Tb 4*f* shell results in a Gd-like state, which is known to have negligible MCA. Adding one 4*f* electron leads to a Dy-like state with strong confinement of the spins to the basal plane but weak anisotropy within this plane. Therefore, also electron transfer realizing Gd $4f^7$ and Dy $4f^9$ configurations will contribute considerably to a transient change of MCA.

In our experiment we altered the 4*f* state of about 20 % of all atoms. The excitation density may be further enhanced by tuning the valence band structure and pump wavelength combining, *e.g.*, 3*d* and 4*f* metals in alloys or multilayers. We expect similar effects in other high-anisotropy materials where MCA is based on stable orbital states with anisotropic charge distribution. The observed electronic excitations give a new handle to transiently manipulate MCA and provides an alternative way to manipulating the spin system in heat-assisted magnetic recording.

Methods

X-ray absorption at the SCS station

We performed the X-ray absorption experiment at the EuXFEL SCS Instrument[21], making use of the high energy resolution ($E/\Delta E$ = 3500) in the energy range of 1 keV around the Gd and Tb 3*d* to 4*f* resonances. We recorded high resolution X-ray absorption spectra using the X-ray gas monitor (XGM) for measurement of

the incident intensity I_0 and the transmission intensity monitor (TIM) to determine the sample transmission I_T. The XA signals (Fig. 1 and SI) are calculated via $-log(I_T/I_0)$. The time-resolved XA measurements were performed with 350 meV energy and 65 fs time resolution (cross-correlation of optical pump and X-ray probe pulses and jitter between pump and probe pulses). For longer intervals of data recording the time resolution was 100 – 200 fs (data shown in Fig. 2).

We studied polycrystalline transmission samples of 10 nm thickness. To prevent oxidation, the rare earth metal was sandwiched between Y-layers. The samples were grown on an Al heat sink on a silicon nitride membrane, Y(2)/RE(10)/Y(25)/Al(300)/SiN(100), RE = Tb and Gd. Numbers in brackets give the layer thickness in nanometers. The Tb and Gd samples were measured at room temperature in the paramagnetic phase. For exciting the samples, we used 800-nm optical pulses (hv = 1.55 eV) from the SASE3 PP laser system. The incident pump fluence was 10 ± 2 mJ/cm². The laser spot size was 0.28 x 0.2 mm^2 and thus significantly larger than the X-ray probe beam of 0.1 x 0.1 mm^2 ensuring a homogeneous excitation profile in the X-ray spot.

Atomic multiplet calculations of X-ray absorption spectra

Because of the localized character of the 4*f* states, the shape of the absorption multiplets can be simulated even for laser-excited samples[14]. The atomic multiplet calculations are performed using the Quanty simulation package[22–24]. For our approach in treating the X-ray absorption cross-section, it is assumed that for 4*f* rare earth compounds the 4*f*-4*f* as well as the 3*d*-4*f* two-particle interactions are most important for the description of the $M_{4,5}$ (3*d*) X-ray absorption spectrum. Due to the large wave-function overlap the dipole term is dominated by $4f^n$ to $3d^9\,4f^{n+1}$ transitions. Details on the quantum chemical treatment of the atomic multiplet calculations of X-ray absorption spectra can be found in Sec. 4 and 5 of the SI as well as in the book by de Groot and Kotani[14,25]. The interactions between the 3*d* core and 4*f* states in these atomic multiplet calculations are explicitly taken into account via the so-called Slater-Condon parameters. The Slater-Condon parameters used in this work were taken from Theo Thole's multiplet extension[26] to the Cowan code[27], which underlies the CTM4XAS interface maintained by de Groot *et al.*[25]. The complete set of values can be found in Tab. S1 in the SI. To correct for the Hartree-Fock over-estimation of electron-electron interaction the Slater reduction factors were set to G_{df} = 0.70, F_{df} = 0.80 and F_{ff} = 0.61 for all calculations.

DFT calculations

We performed density functional theory (DFT) calculations, using the full-potential linear augmented plane wave (FP-LAPW) method in the local spin-density approximation (LSDA), as implemented in the programs ELK [28] and WIEN2k [29]. Spin-orbit coupling is crucial in 4*f* systems, where it is stronger than the crystal field, and has been included in the calculations. The full Brillouin zone has been sampled by about

2000 *k*-points. Strong electron-electron correlations present in the Tb 4*f* states were included in terms of the Hubbard correction *U* and Hund's parameter *J* [30]. The DFT+U double counting was treated in the fully localized limit. For *U* = 9 eV and *J* = 0.5 eV we obtain the self-consistent ground state Tb configuration with m_ℓ = 3 and 15-meV MCA. The Tb configuration with m_ℓ = 2 is self-consistently obtained for *U* = 4 eV and *J* = 0.5 eV. In the calculations where the m_ℓ = 2 configuration was enforced without changing *U*, we employed the magnetic force theorem to obtain the MCA through a one-step total energy calculation. For the MCA calculations an increased accuracy of the muffin-tin potential and charge density expansion into spherical harmonics was used, with l_{max} = 14.

Acknowledgements

The authors acknowledge European XFEL in Schenefeld, Germany, for provision of X-ray free-electron laser beamtime at Scientific Instrument SCS and thank the instrument group and facility staff for their assistance. We acknowledge financial support by the Deutsche Forschungsgemeinschaft through CRC/TRR 227 Ultrafast Spin Dynamics (Collaboration of projects A01, A03, A08 and Mercator Fellow), the Bundesministerium für Bildung und Forschung (grant No. 05K19KE2), the Swedish Research Council (VR), the Swedish Infrastructure for Computing (SNIC), the European Union's Horizon2020 Research and Innovation Programme (Grant No. 863155, s-Nebula), the ERDF in the IT4Innovations national supercomputing center - path to exascale (project CZ.02.1.01/0.0/0.0/16_013/0001791) within the OPRDE and project e-INFRA CZ (ID:90140) of the Ministry of Education, Youth and Sports of the Czech Republic, and the Czech Science Foundation (Grant No. 19-13659S). P.S.M., R.Y.E and M.B. were supported by the Helmholtz Association grant VH-NG-1105.

Author Contributions

The proposal for this study stems from N.T.-K. and C.S.-L. C.S.-L. and M.W. declare equal contributions to this work. Samples were prepared by T.A. The experiment was carried out by N.T.-K., T.A., W.B., S.J., N.P., R.Y.E., P.S.M., M.B., B.E. van K., M.T., R.E.C., L.M., A.Y., G.M., L. Le G., N.A., R.G., M.W. and C.S.-L. Experimental data analysis was carried out by N.T.-K., R.Y.E., T.A. and N.P. with input from M.B., P.S.M., C.S.-L. and M.W. Simulation of multiplet excitations was done by P.S.M., D.L., C.K. and P.M.O. performed the MCA calculations. Electron temperature was simulated by U.A. Manuscript was prepared by N.T.-K., C.S.-L. and M.W. with input from all coauthors.

References

1. Reinsel, D., John Gantz, J., Rydning, J. Data age 2025: The Digitization of the World, From Edge to Core. IDC white paper, Seagate https://www.seagate.com/files/www-content/our-story/trends/files/dataage-idc-report-final.pdf
2. Challener, W., Peng, C., Itagi, A. *et al.* Heat-assisted magnetic recording by a near-field transducer with efficient optical energy transfer. *Nature Photon* **3,** 220–224 (2009). https://doi.org/10.1038/nphoton.2009.26
3. Jensen, J. & Mackintosh, A. R. Rare Earth Magnetism, Clarendon Press, Oxford (1991).
4. Matlak, J., Rismaniyazdi, E. & Komvopoulos, K. Nanostructure, structural stability, and diffusion characteristics of layered coatings for heat-assisted magnetic recording head media. *Sci. Rep.* **8,** 9807 (2018). https://doi.org/10.1038/s41598-018-27688-4
5. Frietsch, B., Donges, A., Carley, R. *et al*., The role of ultrafast magnon generation in the magnetization dynamics of rare-earth metals. *Science Advances* **6**, eabb1601 (2020). https://doi.org/10.1126/sciadv.abb1601
6. Kimel, A.V., Kalashnikova, A.M., Pogrebna, A. & Zvezdin, A.K. Fundamentals and perspectives of ultrafast photoferroic recording. *Physics Reports* **852**, 1-46 (2020). https://doi.org/10.1016/j.physrep.2020.01.004
7. Stanciu C. D., Hansteen, F., Kimel, A. V., Kirilyuk, A., Tsukamoto, A., Itoh, A. and Rasing, T. All-Optical Magnetic Recording with Circularly Polarized Light, *Phys. Rev. Lett.* **99**, 047601 (2007). https://doi.org/10.1103/PhysRevLett.99.047601
8. Kimel, A.V., The Magnetism Roadmap, Chapter 5. All-optical magnetization reversal, *J. Phys. D: Appl. Phys.* **53** (2020) 453001. https://doi.org/10.1088/1361-6463/ab9d98
9. Schlauderer, S., Lange, C., Baierl, S. *et al.* Temporal and spectral fingerprints of ultrafast all-coherent spin switching. *Nature* **569,** 383–387 (2019). https://doi.org/10.1038/s41586-019-1174-7
10. Boeglin, C., Beaurepaire, E., Halté, V., López-Flores, V., Stamm, C., Pontius, N., Dürr, H. A. & Bigot, J.-Y. Distinguishing the ultrafast dynamics of spin and orbital moments in solids, *Nature* **465**, 458 – 461 (2010). https://doi.org/10.1038/nature09070
11. Abdelouahed, S. and M. Alouani, M. Magnetic anisotropy in Gd, GdN, and $GdFe_2$ tuned by the energy of gadolinium 4f states. *Phys. Rev. B* 79, 054406 (2009). https://doi.org/10.1103/PhysRevB.79.054406
12. O'Handley R.C., "Modern magnetic materials", Wiley (2000) page 192. https://doi.org/10.1063/1.1709631
13. Anisimov, S.I., Kapeliovich, B.L. & Perelman, T.L. Electron emission from metal surfaces exposed to ultrashort laser pulses. *Sov. Phys.-JETP* **39**, 375–377 (1974)
14. de Groot, F. & Kotani, A. *Core Level Spectroscopy of Solids*. (CRC Press, 2008).
15. Bovensiepen, U., Coherent and incoherent excitations of the Gd (0001) surface on ultrafast timescales, *J Phys-Condens Mat* **19**, 083201 (2007). https://doi.org/10.1088/0953-8984/19/8/083201

16. Lang, J.K., Baer, Y & Cox, P.A. Study of the 4f and valence band density of states in rare-earth metals: II. Experiment and results. *J. Phys. F: Met. Phys.* **11,** 121–138 (1981). https://doi.org/10.1088/0305-4608/11/1/015
17. van der Laan, G., Arenholz, E., Hu Z. *et al.* Magnetic circular dichroism in Tb 3d to 4f resonant photoemission, Phys. Rev. B **59**, 8835–8843 (1999). https://link.aps.org/doi/10.1103/PhysRevB.59.8835
18. Töws, W. & Pastor, G. M. Many-Body Theory of Ultrafast Demagnetization and Angular Momentum Transfer in Ferromagnetic Transition Metals. *Phys. Rev. Lett.* **115**, 217204 (2015). https://doi.org/10.1103/PhysRevLett.115.217204
19. Bergeard, N., López-Flores, V., Halté, V. *et al.* Ultrafast angular momentum transfer in multisublattice ferrimagnets. *Nat Commun* **5,** 3466 (2014). https://doi.org/10.1038/ncomms4466
20. Hennecke, M., Radu, I., Abrudanel, R. *et al.* Angular Momentum Flow During Ultrafast Demagnetization of a Ferrimagnet. *Phys. Rev. Lett.* **122**, 157202 (2019). https://doi.org/10.1103/PhysRevLett.122.157202
21. Tschentscher, T., Bressler, C., Grünert, J. *et.al.* Photon Beam Transport and Scientific Instruments at the European XFEL. *Appl. Sci.* **7**, 592 (2017). https://doi.org/10.3390/app7060592
22. Haverkort, M. W., Zwierzycki, M. & Andersen, O. K. Multiplet ligand-field theory using Wannier orbitals. *Phys. Rev. B* **85**, 165113 (2012). https://link.aps.org/doi/10.1103/PhysRevB.85.165113
23. Haverkort, M. W., Sangiovanni, G., Hansmann, P. *et al.* Bands, resonances, edge singularities and excitons in core level spectroscopy investigated within the dynamical mean-field theory. *EPL* **108**, 57004 (2014). https://doi.org/10.1209/0295-5075/108/57004
24. Haverkort, M. W. Quanty for core level spectroscopy - excitons, resonances and band excitations in time and frequency domain. *J. Phys. Conf. Ser.* **712**, 012001 (2016). https://doi.org/10.1088/1742-6596/712/1/012001
25. de Groot, F. Multiplet effects in X-ray spectroscopy. *Coord. Chem. Rev.* **249**, 31–63 (2005). https://doi.org/10.1016/j.ccr.2004.03.018
26. Thole, B. T., Cowan, R. D., Sawatzky, G. A., Fink, J. & Fuggle, J. C. New probe for the ground-state electronic structure of narrow-band and impurity systems. *Phys. Rev. B* **31**, 6856(R)–6858 (1985). https://doi.org/10.1103/PhysRevB.31.6856
27. Cowan, R. D. *The Theory of Atomic Structure and Spectra*. (University of California Press, 1981).
28. https://elk.sourceforge.io/
29. P. Blaha, K. Schwarz, G. K. H. Madsen, D. Kvasnicka, J. Luitz, R. Laskowski, F. Tran, and L. D. Marks, WIEN2k, An Augmented Plane Wave + Local Orbitals Program for Calculating Crystal Properties (Techn. Universität Wien, Austria, 2018). http://www.wien2k.at/reg_user/textbooks/usersguide.pdf
30. V. I. Anisimov, J. Zaanen, O. K. Andersen, Band theory and Mott insulators: Hubbard U instead of stoner I. *Phys. Rev. B* **44**, 943–954 (1991). https://doi.org/10.1103/PhysRevB.44.943

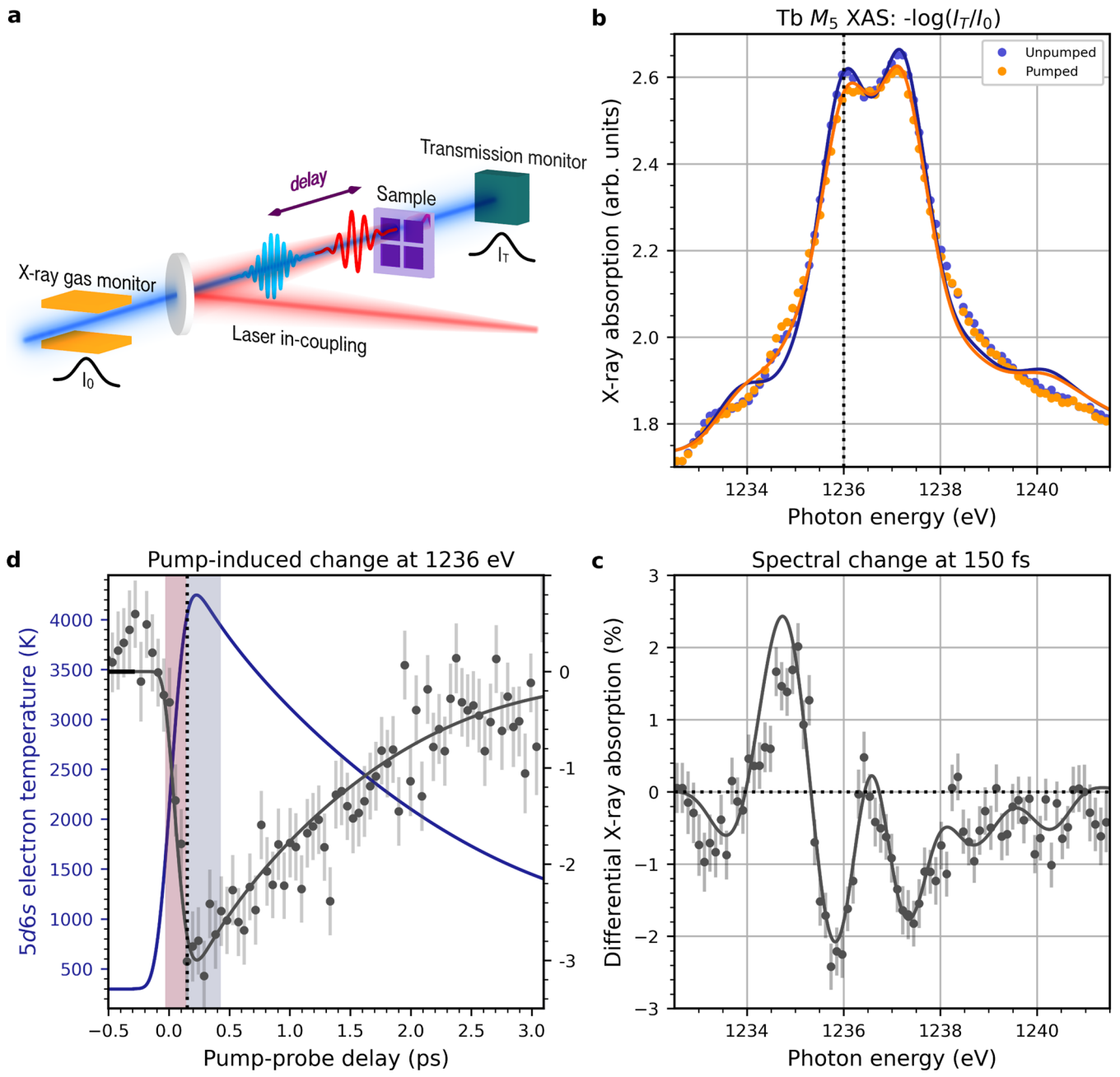

Figure 1 | **Pump-induced changes in the Tb M_5 multiplet.**

a, Sketch of the X-ray absorption experiment. Following excitation with 1.55-eV photons transient X-ray absorption – *log(I_T/I_0)* is probed at the Tb M_5 edge in transmission geometry with 350 meV energy and 65 fs time resolution. The X-ray gas monitor is used to measure the incident intensity I_0, the transmission intensity monitor to determine the sample transmission I_T.

b, XA spectrum of the Tb $3d_{5/2}$ to $4f$ transition (M_5 edge) 150 fs after optical excitation (orange dots) in comparison to the XA spectrum for the unpumped sample (blue dots)

c, Differential X-ray absorption. i.e. the relative change of the XA signal between pumped and unpumped sample.

Solid lines in Figs. 1b and c are fits to the data based on calculations of XA spectra of the $^7F_6$ ground-state (blue), with admixtures of $4f^7$ (3 % $^8S_{7/2}$), $4f^8$ (20 % $^7F_5$) and $4f^9$ (4 % $^6H_{15/2}$) excited state multiplets (orange) and their difference (black).

d, Differential XA signal (black data points) as a function of pump-probe delay measured at a photon energy of 1236 eV. The black solid line is an estimate of the transient XA signal based on the Fermi distribution $f(T_e)$ of excited electrons (see text). The electron temperature T_e (blue solid line) has been calculated by the two-temperature model (see SI).

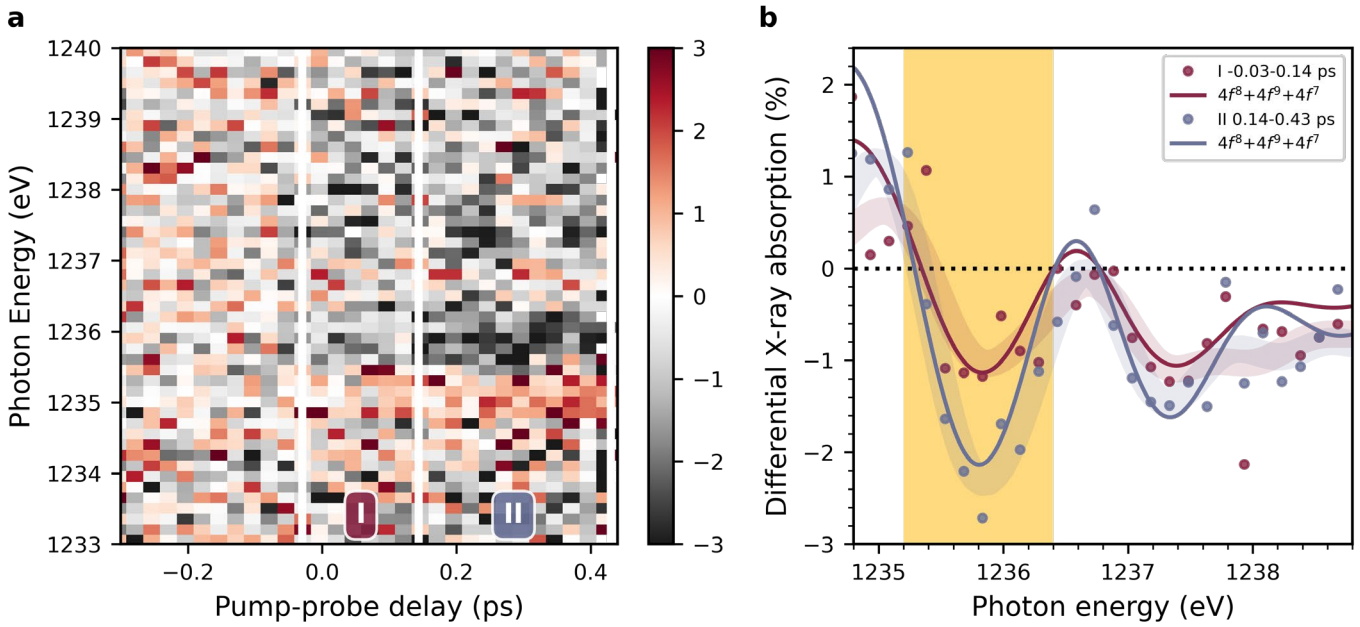

Figure 2 | **Pump-probe delay dependent changes in the Tb M_5 excitation multiplet.**

a, Map of differential X-ray absorption over energy and pump-probe delay. Due to the longer time interval of data recording the resolution is 100 – 200 fs.

b, Energy-dependent differential absorption (dots) at the Tb M_5-edge for the two different pump-probe delay-intervals indicated by the white vertical lines in panel a). Light blue and red filled areas are guides to the eye (for error bars see SI, Fig. S2). The solid lines are simulations including increasing $4f^7$ and $4f^9$ electron-transfer contributions between delay range (I) and (II) (see text and SI).

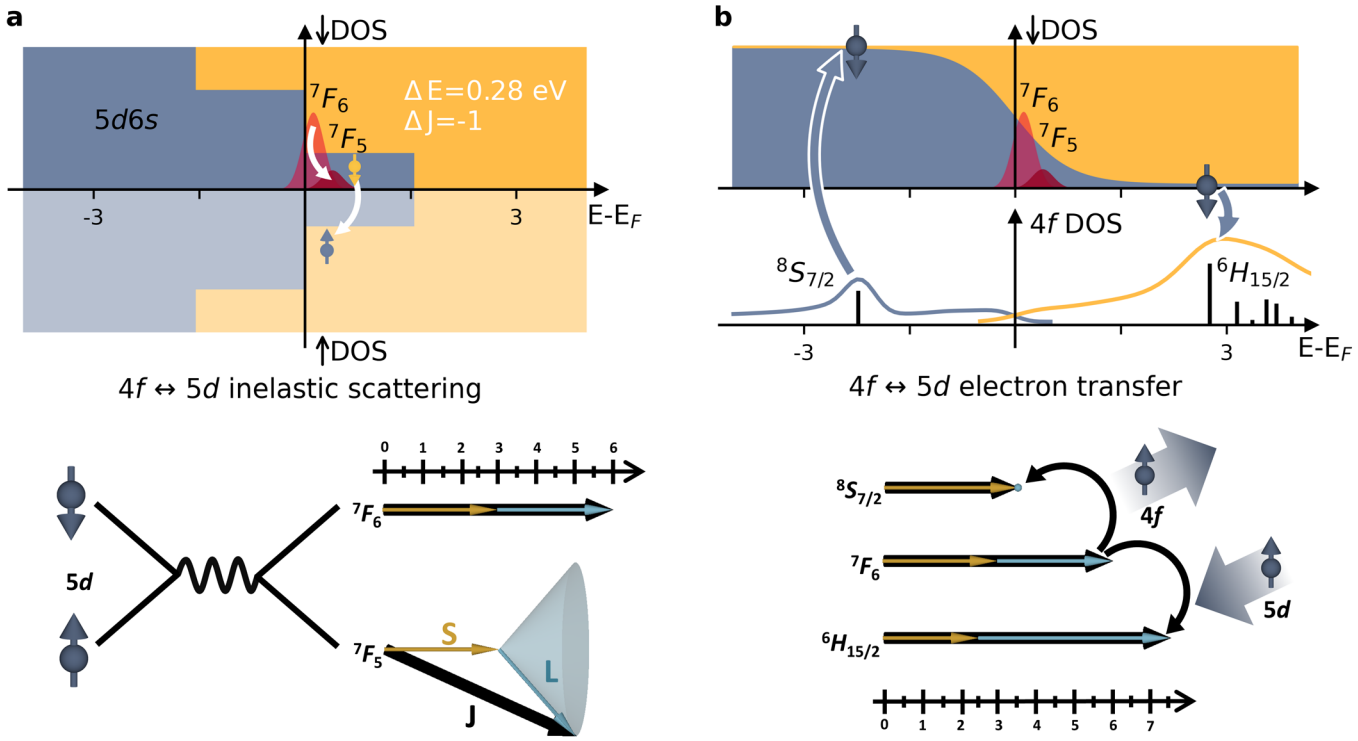

Figure 3| Schematics of optically induced 5*d*-4*f* electronic interactions in Tb.

a, **Inelastic 5*d*-4*f* scattering.** Spin flip scattering (ΔS = +1) of 5*d* valence electrons photo-excited in the interval of ± 1.55 eV around E_F promotes a transition from the Tb $^7F_6$ ground state to the lowest excited $^7F_5$ multiplet. Orbital momentum and energy transfer are ΔJ = -1 and 280 meV, respectively.

b, Quasi-elastic 5*d*-4*f* electron transfer. Within 100 fs after optical excitation 5*d* valence electrons form a hot Fermi distribution (dark grey area). Besides $^7F_5$ contributions from inelastic 5*d*-4*f* scattering, 5*d*-4*f* electron transfer can lead to $4f^7$ and $4f^9$ final states. The lower panel shows the $^8S_{7/2}$ final state of photoemission at 2.3 eV below E_F and the $^6H_{15/2}$ final state of inverse photoemission at 2.8 eV above E_F [16]. Vertical bars stem from multiplet calculations (see text). Excited states reached by processes **a** and **b** are illustrated at the bottom of each figure. Upon electron transport spin and angular momentum change significantly.

Supplementary Information

1. Reference measurement on Gd

In order to check that no other effects may have interfered in the Tb experiment (like an interaction of the sample with the X-ray pulses) we did a reference experiment for Gd, which has the same crystalline and valence band structure as Tb, but differs in the 4f occupation. The lowest orbital excitation within the half-filled Gd $4f^7$ shell multiplet requires an energy of 4.1 eV. Similarly, an electron-transfer excitation of a 5*d* electron to reach the $4f^8$ state takes 4.3 eV and the excitation of a 4*f* electron into the 5*d* manifold would require 8.0 eV ($4f^6$ final state)[1]. Hence all excitation energies are much higher in Gd than in Tb so that multiplet excitations and charge-transfer processes must become significantly weaker. Indeed, for Gd pumped with a fluence identical to Tb we see no change of the absorption spectrum. Within our experimental accuracy the two XA spectra in Fig. S1 recorded before excitation with the pump pulse (unpumped) and averaged over a delay range of 0-200 fs are identical. We can hence safely exclude that the effects seen in Tb are caused by something not related to the Tb electronic structure.

2. Differential X-absorption

Figure S2 reproduces the differential X-absorption from Fig. 2b (main text) including error bars. Data in a) and b) were recorded in successive delay intervals I and II, respectively. We note that the dip at a photon energy of 1235.8 eV becomes more pronounced with time while the one at 1237.5 eV changes only slightly. For energies around 1235 eV we find the absorption to increase with delay. Obviously the 4*f* state evolves in time.

3. Simulation of electron temperature using the two-temperature model

When a metallic thin film is subjected to a near infrared laser pulse, only the electrons are excited by the photon electric field. Initially, the absorbed energy is barely transferred to the lattice and consequently the electron system heats up. The electron and phonon temperatures, T_{el} and T_{ph}, are decoupled for up to several picoseconds until the electron-phonon interaction equilibrates the two heat baths. This phenomenology is well captured by the so-called two-temperature model (2TM)[2,3] which can be written as two coupled differential equations:

$$C_{\mathrm{el}} \frac{\partial T_{el}}{\partial t} = -g_{ep}\left(T_{el} - T_{ph}\right) + \nabla \cdot k\kappa_{el} \nabla T_{el} + P_{laser}(t,z) \quad (1)$$

$$C_{ph} \frac{\partial T_{ph}}{\partial t} = +g_{ep}\left(T_{el} - T_{ph}\right) \quad (2)$$

The parameters entering Eqs. (1) and (2) are material dependent. For Tb thin films we use for the electron specific heat $C_{el} = \gamma_{el} T_{el}$, where[4] $\gamma_{el} = 2.25 \cdot 10^2$ J / m^{3}K^2. As for the phonon specific heat we use the Einstein model[5]:

$$C_{ph} = C_{ph}^{\infty} \left(\frac{T_E}{T_{ph}}\right)^2 \frac{e^{T_E/T_{ph}}}{(e^{T_E/T_{ph}}-1)^2} \quad (3)$$

where T_E is the so-called Einstein temperature. The Einstein model is sufficiently accurate for temperatures higher than the Debye temperature, T_D. Both, Einstein and Debye models provide very similar values for $T_E = 0.75\, T_D$, where $T_D = 174$ K and $C_{ph}^{\infty} = 2.2 \cdot 10^6$ J / m^3 K (Refs. 3 and 6). According to Ref. 7 the electron-phonon coupling is $g_{ep} = 2.5 \cdot 10^{17}$ J / m^3 K. For metallic layers, the heat dissipation at room temperature is usually dominated by electron transport. The thermal conductivity κ_{el} is temperature dependent, increasing for the transient, high electron temperature according to $\kappa_{el} = \kappa_0\, T_{el}/T_{ph}$ [6]. The thermal conductivity is $\kappa_0 = 16$ W / m K [8] and the initial temperature is $T_0 = 300$ K.

Estimation of the absorbed power

In Eq. (1)

$$P_{\text{laser}}(t,z) = \frac{AF_0}{d} \frac{\exp\left(-t^2/2\tau^2\right)}{\sqrt{2\pi}\tau} \exp\left(-\alpha_{\text{opt}}\, z\right) \quad (4)$$

represents the absorbed power density by the electron system, coming from the pump pulse. The laser duration is assumed to be $\tau = 85$ fs, which corresponds to a full width at half maximum of FWHM ~200 fs. The FWHM accounts for the internal thermalization of the electron gas via electron-electron scattering, which practically corresponds to a convolution of the 30 fs laser pulse with a 200 fs Gaussian. In Eq. (4), F_0 is the incidence fluence, d layer thickness, and A absorption coefficient. The attenuation length of the laser is significantly increased by ballistic electron excitation, which is estimated as $\alpha_{\text{opt}}^{-1} = 40$ nm in Tb [8]. We can define the maximum power absorbed, P_0, which happens at $t = 0$ and $z = 0$ (surface layer):

$$P_0 = P_{\text{laser}}(t=0, z=0) = \frac{AF_0}{d\sqrt{2\pi}\tau} \quad (5)$$

The total absorbed energy density can be calculated by integrating $P_{\text{laser}}(t,z)$ over time. For example, at the surface $E_{\text{abs}} = \int P_{\text{laser}}(t, z=0)\, dt = \frac{AF_0}{d}$.

From the experiment we estimate $E_{\text{abs}}(z=0) \sim 3000$ J/cm^3. In the absence of any other dissipation channel the peak temperature can be estimated as

$$T_{\text{el,peak}}^2 = T_0^2 + \frac{2AF_0}{d\gamma_{\text{el}}}. \quad (6)$$

For the case considered here $T_{\mathrm{el,peak}} \sim$ 5200 K. In the presence of electron-phonon coupling and thermal transport, the peak temperature reduces to $T_{\mathrm{el,peak}} \sim$ 4300 K, for the parameters considered here. The total absorbed energy per unit area reduces to the integration over the sample, from z = 0 to z = d and over time.

$$E_{\mathrm{abs}} = \frac{AF_0}{d}\frac{\left(1-\exp(-\alpha_{\mathrm{opt}}d)\right)}{\alpha_{\mathrm{opt}}} \ . \tag{7}$$

Electron-phonon relaxation time

In a first step, one can estimate the electron-phonon relaxation time, $\tau_{\mathrm{ep}} = C_{\mathrm{el}}/g_{\mathrm{ep}}$ from Eq. (1) by assuming that $C_{\mathrm{el}}(T_{\mathrm{el}}) \sim \gamma_{\mathrm{el}}\ (T_0 + \Delta T_{\mathrm{el}}/2)$. For $\Delta T_{\mathrm{el}}/2 \ll T_0$ we can write $\tau_{\mathrm{ep}} = \gamma_{\mathrm{el}}\,\Delta T_{\mathrm{el}}/2g_{\mathrm{ep}}$. For fixed electron-phonon coupling g_{ep} and Sommerfeld coefficient γ_{el}, the relaxation time is defined by the peak temperature. As the peak temperature increases, the electron-phonon relaxation time increases. Thus, for a lower laser power the recovery $\sim \tau_{\mathrm{ep}}^{-1}$ is faster.

Comparison to XAS

From the 2TM, we directly obtain the dynamics of the electronic temperature, T_{el}. Generally, we assume that all electrons of the Fermi distribution above $E_0 - E_F$ = 270 meV can lead to a population of the state at E_0. Thus, the excitation of this state will be proportional to the number of electrons above E_0. We neglect a variation of the density of states and assume a constant DOS. Hence, the number of electrons is proportional to the integral over the Fermi function from E_0 to infinity:

$$g(E_0, T_{\mathrm{el}}) = \int_{E_0}^{\infty} f(E, T_{\mathrm{el}})\, dE \tag{8}$$

where $f(E, T_{\mathrm{el}})$ is the Fermi distribution. Hence,

$$g(T_{\mathrm{el}}) = k_B\, T_{\mathrm{el}} \ln(\exp(-E_0/k_B\, T_{\mathrm{el}}) + 1) \tag{9}$$

where $E_0/k_B = 3133.2$ K. In the low temperature limit $T_{\mathrm{el}} \ll E_0/k_B$, Eq. (9) reduces to the thermal energy weighted by a Boltzmann factor $g(T_{\mathrm{el}}) = k_B\, T_{\mathrm{el}} \exp(-E_0/k_B\, T_{\mathrm{el}})$. Since the scaling factor between the differential X-ray absorption signal $P(t)$ and $g(t)$ is unknown we normalized $g(T_{\mathrm{el}})$ such that $\Delta g_{\mathrm{max}} = P_{\mathrm{max}}$. In particular, we obtain $P = 1 - 0.03\frac{g(t)}{g_{\mathrm{max}}(t)}$.

In Fig. 1c we compare the temporal evolution of the change in 4*f* absorption at 1236 eV (left ordinate, black) with the electron temperature T_e (right ordinate, blue) after laser excitation. We calculated T_e with a two-temperature model. With an absorbed energy of about 3000 J/cm^3 (incidence pump fluence of 10 mJ/cm^2) we reach a maximal T_e of around 4300 K (see Fig. 1c and SI, Fig. S5). Comparing both signals, we see that the decay of T_e is somewhat slower than the decay of the XA difference signal. This discrepancy can be explained by the fact that we measure the electron temperature with a "hot thermometer", namely the first excited

multiplet state $^7F_5$. Only inelastic decay of 5*d* electrons with energy E-$E_F \geq E_1$ = 280 meV provides the energy to excite the 4*f* multiplet. Assuming for simplicity a constant density of states this number of electrons is proportional to $T_e \cdot ln(exp(-E_1/k_BT_e) + 1)$. The solid black line in Fig. 1c shows already a conclusive match to the XA data applying this simple scaling to T_e. It corroborates that 5*d* electrons excited above E_1 contribute substantially via inelastic decay to excitation of the $^7F_5$ multiplet.

Atomistic multiplet calculations

The Schrödinger equation of a free atom contains the kinetic energy of the electrons ($p^2/2m$), the electrostatic interaction of the electrons with the nucleus (Ze^2/r), the electron-electron repulsion (e^2/r) and the spin-orbit coupling of each electron (l.s)[9]:

$$H_{ATOM} = \sum_N \frac{p_i^2}{2m} + \sum_N \frac{-Ze^2}{r_i} + \sum_{pairs} \frac{e^2}{r_{ij}} + \sum_N \zeta(r_i) l_i \cdot s_i \qquad (10)$$

The kinetic energy and the electrostatic interaction of the electrons with the nucleus are the same for all electrons in a given atomic configuration. They define the average energy of the configuration (H_{av}). The electron-electron repulsion and the spin-orbit coupling define the relative energy of the different terms within a configuration, for example leading to the Hund's rule assignment of the electronic ground state configuration. The electron-electron repulsion is very large, but the spherical average of the electron-electron interaction can be separated from the non-spherical part. The spherical average can then be added to H_{av}. Overall this H_{av} is neglected in the atomic multiplet simulations of X-ray absorption: the difference between H_{av} in the initial and final state of the X-ray absorption process defines the energy shift needed in the calculation to fit to the experimental absorption spectrum. The modified electron-electron Hamiltonian plus the spin-orbit coupling part determine the energies of the different terms within the atomic configuration in both the initial and final state of the X-ray absorption process. The terms of a configuration are indicated by their total orbital moment *L*, spin moment *S* and total moment *J* in a $^{2S+1}L_J$ format. The general formulation of the matrix elements of two-electron wave functions can be written as:

$$\left\langle {}^{2S+1}L_J \left| \frac{e^2}{r_{12}} \right| {}^{2S+1}L_J \right\rangle = \sum_k f_k F^k + \sum_k g_k G^k \qquad (11)$$

F^i(f_i) and G^i(g_i) are the Slater-Condon parameters for, respectively, the radial (angular) part of the direct Coulomb repulsion and the Coulomb exchange interaction. The f_i and g_i are non-zero only for certain integer values of *k* (running from 0 or 1 to *i*), depending on the configuration. The direct Coulomb repulsion f_0 is always present and the maximum value *i* equals two times the lowest value of ℓ. The exchange interaction Slater-Condon parameter g_i is present only for electrons in different shells (as in our case 3*d* and 4*f*). For g_k, *k* is even if $\ell_1 + \ell_2$ is even and *k* is odd if $\ell_1 + \ell_2$ is odd (ℓ_1 = 2, ℓ_2 = 3 for $3d^9 4f^{n+1}$). The maximum value *i* equals

$\ell_1 + \ell_2$. A $4f^n$ configuration contains f_0, f_2, f_4 and f_6 Slater-Condon parameters, because $\ell = 3$ for a 4*f* electron, thus the maximum value is 6. The final state in X-ray absorption with the $3d^9\,4f^{n+1}$ configuration contains f_0, f_2, f_4, f_6 (for direct 4*f*-4*f* interaction) and f_2, f_4 (for 3*d*-4*f* interaction) and g_1, g_3 and g_5 Slater-Condon parameters.

Table S1. Hartree-Fock values (before Slater reduction) for Slater-Condon parameters for different rare-earth electron configurations: f_i parameters are shown for direct 4*f*-4*f* (f_i (*ff*)) and direct 3*d*-4*f* (f_i (*df*)) interactions (all values in eV).

	Tb $4f^7$	**Tb $4f^8$**	**Tb $4f^9$**	**Gd $4f^6$**	**Gd $4f^7$**	**Gd $4f^8$**
f_2 (ff)	15.829	14.915	13.892	15.438	14.505	13.452
f_4 (ff)	9.981	9.360	8.670	9.737	9.103	8.394
f_6 (ff)	7.195	6.734	6.225	7.020	6.550	6.026
4f spin-orbit coupling	0.237	0.221	0.205	0.213	0.197	0.182
	Tb $3d^9 4f^8$	**Tb $3d^9 4f^9$**	**Tb $3d^9 4f^{10}$**	**Gd $3d^9 4f^7$**	**Gd $3d^9 4f^8$**	**Gd $3d^9 4f^9$**
f_2 (ff)	16.461	15.586	14.620	16.086	15.197	14.210
f_4 (ff)	10.390	9.794	9.141	10.157	9.551	8.884
f_6 (ff)	7.493	7.050	6.567	7.325	6.876	6.383
4f spin-orbit coupling	0.268	0.251	0.234	0.242	0.225	0.209
3d spin-orbit coupling	13.363	13.368	13.372	12.352	12.357	12.361
f_2(df)	10.631	10.055	9.468	10.303	9.715	9.114
f_4(df)	5.013	4.709	4.406	4.843	4.533	4.223
g_1(df)	7.730	7.240	6.755	7.451	6.951	6.457
g_3(df)	4.535	4.245	3.959	4.370	4.075	3.783
g_5(df)	3.133	2.933	2.735	3.019	2.815	2.613

The value for f_0 for the $4f^n$ initial state was based on the reduced f_2, f_4 and f_6 parameters:

$$f_0(ff) = (4/195) \cdot f_2 + (2/143) \cdot f_4 + (100/5577) \cdot f_6$$

The values for f_0 for the $3d^9 4f^n$ x-ray absorption final state were (considering the interactions of 4*f*-4*f* electrons and 3*d*-4*f* electrons) based on the reduced f_2, f_4 and f_6 and g_1, g_3 and g_5 parameters:

$$f_0(ff) = (4/195) \cdot f_2 + (2/143) \cdot f_4 + (100/5577) \cdot f_6$$

$$f_0(df) = (3/70) \cdot g_1(df) + (2/105) \cdot g_3(df) + (5/231) \cdot g_5(df)$$

The Slater-Condon parameters used in this work were taken from Theo Thole's multiplet extension[10] to the Cowan code[11], which underlies the CTM4XAS interface maintained by de Groot et al.[12,13]. The complete set

of values is listed in Table S1 including the 4*f* spin-orbit coupling ζ. To correct for the Hartree-Fock over-estimation of electron-electron interaction the Slater reduction factor were set to G_{df}=0.70, F_{df}=0.80 and F_{ff}=0.61 for all calculations, i.e., the g_1(df), g_3(df) and g_5(df) are multiplied by G_{df}, f_2(df), f_4(df) are multiplied by F_{df} and the f_2(ff), f_4(ff) and f_6(ff) for both the initial $4f^n$ configurations and $3d^9 4f^{n+1}$ configurations are multiplied by F_{ff}.

4. Calculation of X-ray absorption spectra at the Tb M_5 and M_4 edges

We use the Quanty routine for X-ray absorption calculations[14-16]. Calculations were done with so-called lua-input-files and an example of such an input-file is shown in Table S4 at the end of the SM.

Fig. S2 shows calculated X-ray absorption spectra at the Tb M_5 and M_4 edges. The spectroscopic notation $^{2S+1}L_J$ describes the electron configuration of the 4*f* shell before the XA probe step (without 3*d* core hole). The turquoise spectrum at the bottom of Fig. S2 shows excitations from the $3d_{5/2}$ and $3d_{3/2}$ core level to the $4f^8$ ground state (GS), i.e., the initial $^7F_6$ configuration with m_ℓ = 3 at around 1235 and 1255 eV, respectively. We fitted the measured ground state (GS) spectrum with the calculated GS spectrum with respect to energetic position and an experimental Gaussian broadening. The six subsequent spectra are X-ray transitions to excited 4*f* states where orbital momentum *L* = 3 and spin *S* = 3 become canted. For the different orientations, described with m_ℓ = 2, 1, 0, -1, -2, -3 and fixed m_s = 3 we obtain total angular momenta of *J* = 5, 4, 3, 2, 1, 0, respectively. The $^5D_4$ multipet corresponds to the first spin-flip excitation within the $4f^8$ configuration resulting in *S* = 2 and *L* = 2 aligned to yield *J* = 4. The energies required to excite these multiplets by 4*f* inner-shell transitions are listed in Tab. S2. We aligned all spectra on the global energy scale applying the shift determined for the GS.

The two spectra at the top describe X-ray transitions into the two lowest charge-transfer states. The $4f_7\,^8S_{7/2}$ configuration corresponds to the transfer of a 4*f* electron into an empty 5*d* state. This requires excited holes at an energy of about 2.3 eV below the Fermi level E_F, which corresponds to the lowest ionization energy of the 4*f* state, i.e. the single $^8S_{7/2}$ multiplet component in X-ray photoelectron spectroscopy[17]. The $4f^9\,^6H_{15/2}$ configuration is reached by transfer of a 5d valence electron into the 4f shell. For this, electrons have to transiently occupy valence-band states at an energy of 2.8 eV above E_F, which corresponds to the lowest 4*f* excitation in Bremsstrahlung Isochromat spectroscopy[17].

Table S2: Excitation energies (E_i in eV) oft the first seven inner shell excitations.

GS	E_1	E_2	E_3	E_4	E_5	E_6	E_7
$^7F_6$	$^7F_5$	$^7F_4$	$^7F_3$	$^7F_2$	$^7F_1$	$^7F_0$	$^5D_4$
0	0.28	0.41	0.54	0.62	0.68	0.71	1.71

5. Simulation of X-ray absorption spectra at the Tb M_5 edge

In the x-ray absorption experiment we measured the intensity of the incoming X-rays I_0 and of the signal I_T transmitted through the sample. As X-ray absorption we evaluate the extinction $XA = -ln(I_T/I_0)$. For simulation of the pump-induced effect on the Tb M_5 absorption spectrum, as a first step the XA signal in equilibrium for the unpumped sample is described by atomic calculations (see Section 3 and 4, SI). The calculations deliver the imaginary part of the scattering amplitude *f*, which corresponds to the transition probability from the 3*d* ground state to the unoccupied 4*f* state with different 4*f* electronic configuration and on an arbitrarily shifted energy scale *e*. In the case of the *unpumped* signal we fit the *Im*[*f*](e) for the $4f^8$ $^7F_6$ ground state (GS) multiplet to the XA spectrum. Therefore, the energy scale *e* is shifted by *a*

$$E(a) = e + a.$$

By convoluting $Im[f]_{GS}$(E) with a Gaussian function we account for the energy resolution of the experiment and the core-hole lifetime broadening, which delivers the absorption coefficient

$$\mu_{GS}(E) = Im_{GS}(E) \otimes Gauss(\Delta E).$$

The XA signal is

$$XAS_{GS} = I_0\, e^{-\mu_{GS}(E)d} + C + edge\ jump$$

where I_0 and *C* are parameters for scaling. Offset and *d* denotes the sample thickness. The *edge jump* is approximated as a

$$edge\ jump = I_{ej}\, H(E_B) \otimes Gauss(\Delta E_{lifetime})$$

with $H(E_B)$ being a Heaviside-function at the binding energy E_B, scaled by I_{ej} and core-hole life time broadened by convolution with a Gaussian function.

Simulation of the X-ray absorption spectrum for the Tb $4f^8$ ground state

For the fit parameters shown in Table S3 we find the simulation of the *unpumped* spectrum shown in Fig. S5.

Table S3: Parameters for fitting *Im*[*f*](e) for the $4f^8$ $^7F_6$ groundstate (GS) multiplet to the Tb M_5 XA spectrum for the unpumped sample.

a	1247.26 eV	*d*	10e-08 m	*C*	1.725
ΔE	0.41 eV	I_{ej}	0.0644	$\Delta E_{lifetime}$	0.2 eV
I_0	1.5200e+08	E_B	1237.70 eV		

Simulation of pump-induced spectral changes

For the simulation of the pump induced spectral changes, the spectrum for the pumped sample is described by the GS spectrum with admixtures of different excited electronic configurations. Therefore, we write the absorption coefficient for the *pumped* spectrum as

$$\mu_{exc}=(1-\sum_i c_i)\mu_{GS}+\sum_i c_i\mu_i$$

where *i*, indicates the excited 4*f* state, μ_i the respective absorption coefficient and c_i the relative contribution to the total absorption coefficient. The XA signal from the pumped sample is

$$XAS_{exc} = I_0\, e^{-\mu_{exc}(E)d} + C + edgejump$$

with the fit parameters in Table S3 kept constant. The pump effect *P* is described as differential X-ray absorption, i.e., as the relative change of the XA signal in percent.

$$P = 100 \cdot \frac{XAS_{GS} - XAS_{exc}}{XAS_{GS}}$$

For the simulation *P* is fitted with c_i as fit parameters. In the case of $4f^8$ excited states contributing to the signal, we assumed a constant parameter *e* (see Table S3) for the energy position of the multiplet. For $4f^9$ and $4f^7$ electronic configuration a correction of the energy e_s is included, as the multiplets will appear at a varied energy position due to screening of the additional electron/hole in the 4*f* shell. Since the atomic calculations adequately describe the two main features in the GS spectrum at 1236 eV and 1237.2 eV, the fit is performed in the middle region of the spectrum (1234.8 eV-1238.8 eV) denoted by the vertical dotted lines in Fig. S5.

Beginning the simulation of the differential absorption for the dataset recorded at 150 fs pump-probe delay, as a first attempt we considered contributions, only from the lowest excited state $4f^8\,{}^7F_5$. We find reasonable agreement for 15.6% admixture of the ${}^7F_5$ multiplet to the GS, however do not achieve a quantitative description of the experimental data (Fig. S6).

Higher f^8 multiplet excitations

In the next step, higher $4f^8$ excited states are considered. This is first done by assuming a temperature dependent probability for populating higher energetic $4f^8$ states via a Boltzmann distribution $c_i = e^{E_i/k_BT}$, *e.g.*, to account for potential phonon based 4*f* excitation. Here, c_i is the relative contribution of the multiplet *i* at energy E_i (see Table S3). In a second step the relative admixtures of $4f^8$ states are described by scaling them with an integrated Fermi function $c_i = T \cdot log(e^{E_i/k_BT} + 1)$ and hence picturing 4*f* excitations mediated by interaction with the photo-excited 5*d*6*s* valence system.

The best fitting is achieved with a 1540 K Boltzmann distribution and a 1370 K Fermi function, as shown in Fig. S7 and S8, respectively. While the quantitative agreement with the experimental data has partially improved, the resulting temperatures are clearly out of range with respect to the 5*d*6*s* electron and phonon temperature at 150 fs pump-probe delay, deduced from a simulation based on the two-temperature model (see Section 3) and determined to be around 4000 K for electrons and 300 K for phonons (Fig. S3). We hence exclude contributions of higher $4f^8$ excited states.

Electron transfer excitations

However, including the energetically lowest $4f^7$ ($^8S_{7/2}$) and $4f^9$ ($^6H_{15/2}$) multiplets in the simulation improves the fit considerably. The spectral shape itself can readily be simulated and experimentally observed in Gd and Dy, respectively. However, the atomic multiplet calculation depends critically on core-hole screening, which is altered by adding or removing a localized 4*f* electron. We dealt with that by estimating the relative energy positions from the energy separation between the multiplet terms after alignment of the calculated spectra at the first absorption peak assuming metallic screening. Starting in the $4f^8$ ground state the lowest energy peak will be formed by the 3*d* core hole and the 4*f* electron excited into the $m_\ell = 2$ orbital. In the lowest $4f^9$ multiplet state this orbital is already occupied and the lowest state is $m_\ell = 1$, which occurs at higher energy. In turn, an excitation into the $4f^7$ state would require lower energy as the $m_\ell = 3$ state is empty. For metallic screening all 3*d* to 4*f* excitonic transitions should be equally well screened and the differential shifts correspond to the *ff* excitation energies of -0.28 and +0.13 eV (Tab. S2). We used these shifts as starting values for our fit. For the best fit in Figs. 1a and 2b of the main text we arrived at slightly larger shifts of -0.45 and +0.55 eV for the $4f^7$ and $4f^9$ states, respectively. The shifts deduced from fitting the data may be justified by stronger screening of the 3*d* core hole by the localized 4*f* as compared to the delocalized 5*d* electrons. In that case the binding energy of the core exciton is higher in the $4f^7$ and lower in the $4f^9$ state. Within these settings we find 73 % of the $^7F_6$ GS, 20 % of the $^7F_5$, 4 % of the $4f^9$ and 3 % of the $4f^7$ multiplet contributing to the *pumped* absorption spectra at 150 fs pump-probe delay. With a dominant contribution to the excitation of the $4f^8$ $^7F_5$ state, we expect accordingly to the 3rd rule of Thole and van der Laan[9], a decrease of the *pumped* Tb M_5 signal and an increase of intensity at the Tb M_4 resonance. This is in line with the observations in Fig. S9.

For the simulation of the pump effect obtained from cuts through the energy-delay map in Fig. 2a of the main text, we adopted the parameters from Table S3 and the values e_s. Considering $4f^8$ as well as $4f^9$ and $4f^7$ excitations we find the best fits shown in Fig. 2b. Here we use 11.4% $^7F_5$, 1.9 % $4f^9$ and 1.9% $4f^7$ multiplets in interval (I) -0.03-0.14 ps and 19% $^7F_5$, 4.6 % $4f^9$ and 2.8% $4f^7$ in interval (II) 0.14-0.43 ps. The experimental error bars for the differential absorption in Fig. 2b of the main text are shown in Fig. S2.

3rd rule of Thole and van der Laan

We note that the overall XA signal slightly decreases upon laser excitation. In other words, the difference spectrum in Fig. 1c has a negative integral over the M_5 edge. This observation is in line with the 3rd rule of Thole and van der Laan[9], stating for our case that the multiplet with the highest J has the highest intensity $I_J(M_5)$ at the M_5 edge. For the other J levels the branching ratio $I_J(M_5)$ / ($I_J(M_4)$ + $I_J(M_5)$) gradually decreases with J. In accord with our measurements in Fig. S9 exciting predominantly the $^7F_5$ multiplet the intensity at the M_5 edge decreases while the intensity at the M_4 edge increases. The $^7F_5$ contribution leads to a transfer of spectral weight from the M_5 to the M_4 resonance.

6. Time resolution of the experiment

The duration of the optical laser pulse was 30 fs and of the FEL pulse 25 fs. The measured arrival time jitter for small time spans of 10 min was on the order of 50 fs. Combining these numbers gives a temporal resolution of about 65 fs. This is the time resolution of the measurements presented in Fig. 1 of the main text. There were also slower drifts on the order of 100 - 200 fs on longer timescales. We cannot exclude that these shifts contribute to the recorded energy vs. delay map and differential absorption spectra in Fig. 2 of the main text.

7. Samples

We studied polycrystalline transmission samples of 10 nm thickness sandwiched between Y-layers. Samples were grown by molecular beam epitaxy in the combined MBE/SD (sputter deposition) chamber of the PM3 beamline at BESSY II. As substrate we used an Al heat sink on a silicon nitride membrane. The pressure during evaporation was 2 to 7 x 10^{-9} mbar. The stack was Y(2)/RE(10)/Y(25)/Al(300)/SiN(100), where the number indicates the nominal layer thickness in nanometer and RE = Gd or Tb, respectively. Due to different positions of the evaporators with respect to the quartz microbalance, we estimate thickness variations on the order of 30 %.

8. Optical pump fluence

The optical pump- and X-ray probe beams were nearly coaxial and normally incident on the sample. From measured beam power and spot size and the 10 kHz repetition rate we estimate an incident pump fluence of 10 ± 2 mJ/cm^2. The optical constants for crystalline Y (n = 2.13, k = 2.67) and Tb (n = 2.47, k = 3.27) are taken from Ref. 18. For an RE(10)/Y(\infty) stack and normal light incidence we estimate an absorbed power of 16 - 25 % in a 10 ± 3 nm RE layer which corresponds to an absorbed energy of 1.3 – 3 x 10^3 J / cm^3.

9. Transfer of energy density

If we assume that maximal 20 % of all Tb atoms are in the first excited multiplet state, we calculate for a density of 3.12 x 10^{22} atoms/cm^3 a stored energy of 0.27 x 10^3 J/cm^3, which corresponds to about 9 % of the maximum absorbed energy density.

10. Two-photon absorption vs thermal occupation

Two-photon absorption will only contribute to excitation of higher lying multiplets while the pump-pulse excites the sample, i.e., around zero delay. Independent of the initial distribution electrons will still thermalize to a hot Fermi distribution within 100 fs. The temperature of this distribution decays as described in Fig. 1c of the main text and Fig. S1. From this description we expect the highest contribution of $4f^7$ and $4f^9$ multiplet excitations at around 150 - 400 fs where T_{el} ~ 4000 K. The probability to find an electron at $E - E_F$ = 2.7 eV is on the order of 10^{-4}. We note that it is not straight forward to estimate the contribution of two-photon absorption. While single photon absorption scales with the laser-pulse intensity, two photon excitations scale with the square of the intensity. Space charge effects due to the IR pump pulse ($h\nu$ = 1.6 eV) in time-resolved photoemission of Gd set in at an absorbed fluence of 0.5 mJ / cm^2 (~ 10^{15} photons / cm²) [19]. In direct photoemission with VUV pulses we detect in the same setup about 1 electron per 10^8 photons / cm^2 and space charge sets in at only slightly higher photon flux. Thus, we argue that the ratio between two-photon photoemission and direct photoemission must be on the order of 10^{-6} for the fluence range we also used in the present experiment, i.e., an overall contribution of two-photon absorption in the order of 1%.

Table S4: Input file for Quanty calculations (lines starting with "- -" are comment lines).

```
-- Slater integral reduction may be different for different direct Coulomb and exchange, which can be done by beta1(Fff), beta2(Fdf) and beta3(Gdf) :
beta1 = 0.61
beta2 = 0.80
beta3 = 0.7
---- Scale the spin-orbit coupling (for direct comparison to CTM4XAS/TT-multiplet 0.99 is chosen)
zeta = 0.99
-- Relative energy axis for the x-ray absorption spectrum (Emin1,Emax1, NE1a amount of points+1 in spectrum); Gamma0 and Lor0 are the Gaussian and Lorentzian broadening parameters for the x-ray absorption spectrum
Emin1 =-30.0
Emax1 = 40.0
NE1a = 7000
Gamma0 = 0.1
Lor0= 0.1
------- Name of output-files for XAS calculations ----
XASfile0="Tb3MXAS_ES00.dat"
XASfile1="Tb3MXAS_ES01.dat"
XASfile2="Tb3MXAS_ES02.dat"
XASfile3="Tb3MXAS_ES03.dat"
XASfile4="Tb3MXAS_ES04.dat"
XASfile5="Tb3MXAS_ES05.dat"
XASfile6="Tb3MXAS_ES06.dat"
XASfile7="Tb3MXAS_ES07.dat"
------- Settings for Tb local interactions ----------
```

```
-- Nelec is the amount of electrons in the 4f shell; F2ff, F4ff, F6ff are the Slater integral parameters for the direct 4f-4f Coulomb interaction in the initial state; XF2ff, XF4ff and Xf6ff are the Slater integral parameters for the direct 4f-4f Coulomb interaction in the x-ray excited state (final state of x-ray absorption); F2df,F4df are the Slater integral parameters for the direct 3d-4f Coulomb interaction (only present in the XAS final state); G1df,G3df are the Slater integral parameters for the 3d-4f exchange interaction (only present in the XAS final state); zeta_4f and Xzeta_4f are the 4f spin-orbit coupling parameters for the initial and final state of the x-ray absorption process; zeta_3d is the 3d spin-orbit coupling parameter (which becomes effective in the final state of the x-ray absorption process, splitting the M4 and M5 edge)
Nelec=8  - - or Nelec=7 – or Nelec=9
if Nelec==8 then
        F2ff=14.915; F4ff=9.360; F6ff=6.734; zeta_4f=0.221;
        XF2ff=15.586; XF4ff=9.794; XF6ff=7.050; Xzeta_4f=0.251;
        zeta_3d=13.368; F2df=10.055; F4df=4.709; G1df=7.240; G3df=4.245; G5df=2.933;
elseif Nelec==9 then
        F2ff=13.892; F4ff=8.670; F6ff=6.225; zeta_4f=0.205;
        XF2ff=14.620; XF4ff=9.141; XF6ff=6.567; Xzeta_4f=0.234;
        zeta_3d=13.372; F2df=9.468; F4df=4.406; G1df=6.755; G3df=3.959; G5df=2.735;
elseif Nelec==7 then
        F2ff=15.829; F4ff=9.981; F6ff=7.195; zeta_4f=0.237;
        XF2ff=16.461; XF4ff=10.390; XF6ff=7.493; Xzeta_4f=0.268;
        zeta_3d=13.363; F2df=10.631; F4df=5.013; G1df=7.730; G3df=4.535; G5df=3.133;
end
-------- scaling with beta factors (Slater reduction)----------------
-- direct Coulomb ground state (beta1)
F2ff=beta1*F2ff; F4ff=beta1*F4ff; F6ff=beta1*F6ff
-- direct Coulomb p-d excited state (beta2)
F2df=beta2*F2df; F4df=beta2*F4df;
-- exchange p-d (excited state, beta3)
G1df=beta3*G1df; G3df=beta3*G3df; G5df=beta3*G5df
-- direct Coulomb excited state (beta1)
XF2ff=beta1*XF2ff; XF4ff=beta1*XF4ff; XF6ff=beta1*XF6ff
------ scaling with zeta factor (spin-orbit couplings) ----
zeta_3d=zeta*zeta_3d
zeta_4f=zeta*zeta_4f
Xzeta_4f=zeta*Xzeta_4f
------ Number of possible many-body states in the initial configuration (14 f-electrons + 10 d-electrons)
Npsi = math.fact(14) / (math.fact(Nelec) * math.fact(14-Nelec))
NFermion=24
NBoson=0
IndexDn_3d={0,2,4,6,8} -- d-shell [dn]
IndexUp_3d={1,3,5,7,9} -- d-shell [up]
IndexDn_4f={10,12,14,16,18,20,22} -- f-shell [dn]
IndexUp_4f={11,13,15,17,19,21,23}  -- 4f-shell [up]
--- define operators
OppSx   =NewOperator("Sx"   ,NFermion, IndexUp_4f, IndexDn_4f)
OppSy   =NewOperator("Sy"   ,NFermion, IndexUp_4f, IndexDn_4f)
OppSz   =NewOperator("Sz"   ,NFermion, IndexUp_4f, IndexDn_4f)
OppSsqr =NewOperator("Ssqr" ,NFermion, IndexUp_4f, IndexDn_4f)
OppSplus=NewOperator("Splus",NFermion, IndexUp_4f, IndexDn_4f)
OppSmin =NewOperator("Smin" ,NFermion, IndexUp_4f, IndexDn_4f)
OppLx   =NewOperator("Lx"   ,NFermion, IndexUp_4f, IndexDn_4f)
OppLy   =NewOperator("Ly"   ,NFermion, IndexUp_4f, IndexDn_4f)
OppLz   =NewOperator("Lz"   ,NFermion, IndexUp_4f, IndexDn_4f)
OppLsqr =NewOperator("Lsqr" ,NFermion, IndexUp_4f, IndexDn_4f)
OppLplus=NewOperator("Lplus",NFermion, IndexUp_4f, IndexDn_4f)
OppLmin =NewOperator("Lmin" ,NFermion, IndexUp_4f, IndexDn_4f)
OppJx   =NewOperator("Jx"   ,NFermion, IndexUp_4f, IndexDn_4f)
OppJy   =NewOperator("Jy"   ,NFermion, IndexUp_4f, IndexDn_4f)
OppJz   =NewOperator("Jz"   ,NFermion, IndexUp_4f, IndexDn_4f)
OppJsqr =NewOperator("Jsqr" ,NFermion, IndexUp_4f, IndexDn_4f)
OppJplus=NewOperator("Jplus",NFermion, IndexUp_4f, IndexDn_4f)
OppJmin =NewOperator("Jmin" ,NFermion, IndexUp_4f, IndexDn_4f)
Oppldots=NewOperator("ldots",NFermion, IndexUp_4f, IndexDn_4f)
------ Coulomb operator -----------------
OppF0 =NewOperator("U", NFermion, IndexUp_4f, IndexDn_4f, {1,0,0,0})
OppF2 =NewOperator("U", NFermion, IndexUp_4f, IndexDn_4f, {0,1,0,0})
OppF4 =NewOperator("U", NFermion, IndexUp_4f, IndexDn_4f, {0,0,1,0})
OppF6 =NewOperator("U", NFermion, IndexUp_4f, IndexDn_4f, {0,0,0,1})
--------- Spin-orbit coupling in 3d-shell (core=c)--------
Oppcldots= NewOperator("ldots", NFermion, IndexUp_3d, IndexDn_3d)
```

```
------- Core hole potentials -------
---- direct
OppUdfF0 = NewOperator("U", NFermion, IndexUp_3d, IndexDn_3d, IndexUp_4f, IndexDn_4f, {1,0,0}, {0,0,0})
OppUdfF2 = NewOperator("U", NFermion, IndexUp_3d, IndexDn_3d, IndexUp_4f, IndexDn_4f, {0,1,0}, {0,0,0})
OppUdfF4 = NewOperator("U", NFermion, IndexUp_3d, IndexDn_3d, IndexUp_4f, IndexDn_4f, {0,0,1}, {0,0,0})
---- exchange
OppUdfG1 = NewOperator("U", NFermion, IndexUp_3d, IndexDn_3d, IndexUp_4f, IndexDn_4f, {0,0,0}, {1,0,0})
OppUdfG3 = NewOperator("U", NFermion, IndexUp_3d, IndexDn_3d, IndexUp_4f, IndexDn_4f, {0,0,0}, {0,1,0})
OppUdfG5 = NewOperator("U", NFermion, IndexUp_3d, IndexDn_3d, IndexUp_4f, IndexDn_4f, {0,0,0}, {0,0,1})
t=math.sqrt(1/2);
-- setting up the transition operators with various polarisations (dipole x: TXASx, dipole y: TXASy, dipole z: TXASz)
Akm = {{1,-1,t},{1, 1,-t}}
TXASx = NewOperator("CF", NFermion, IndexUp_4f, IndexDn_4f, IndexUp_3d, IndexDn_3d, Akm)
Akm = {{1,-1,t*I},{1, 1,t*I}}
TXASy = NewOperator("CF", NFermion, IndexUp_4f, IndexDn_4f, IndexUp_3d, IndexDn_3d, Akm)
Akm = {{1,0,1}}
TXASz = NewOperator("CF", NFermion, IndexUp_4f, IndexDn_4f, IndexUp_3d, IndexDn_3d, Akm)
--- Input parameters for the Hamiltonian -----
U      =  0.000
F0ff    = U+(4/195)*F2ff+(2/143)*F4ff+(100/5577)*F6ff
XF0ff   = U+(4/195)*XF2ff+(2/143)*XF4ff+(100/5577)*XF6ff
Udf     =  0.000
F0df    =  Udf+G1df*(3/70)+G3df*(2/105)+(5/231)*G5df
--- initial state Hamiltonian
Hamiltonian =  F0ff*OppF0 + F2ff*OppF2 + F4ff*OppF4 + F6ff*OppF6 + zeta_4f*Oppldots
-- final state Hamiltonian
XASHamiltonian = XF0ff*OppF0 + XF2ff*OppF2 + XF4ff*OppF4 + XF6ff*OppF6 +
Xzeta_4f*Oppldots+F0df*OppUdfF0+F2df*OppUdfF2+F4df*OppUdfF4+G1df*OppUdfG1+G3df*OppUdfG3+G5df*OppUdfG5+zeta_3d*Oppcldo
ts
StartRestrictions = {NFermion, NBoson, {"1111111111 00000000000000",10,10}, {"0000000000 11111111111111",Nelec,Nelec}}
-- Finding the initial state ground state and its optically excited states
psiList = Eigensystem(Hamiltonian, StartRestrictions, Npsi)
for key,value in pairs(psiList) do
  stateenergy = value * Hamiltonian * value
  print(key, stateenergy)
end
--XAS spectra calculations: Most initial states have degeneracy, so XAS spectra are calculated in a loop over the degenerate states. The loops
for j=x,xx shown below are the examples for Tb3(4f_8). The start and end value of these loops depend on the 4f_n occupation
SpectraAv = 0
for j=1, 13 do
        TempSpect = CreateSpectra(XASHamiltonian, {TXASx, TXASy, TXASz}, psiList[j], {{"Emin",Emin1}, {"Emax",Emax1}, {"NE",NE1a}})
        SpectraAv = SpectraAv + Spectra.Sum(TempSpect, {1,1,1})/3.
end
Broaden1=Spectra.Broaden(SpectraAv, Gamma0, {{Emin1, Lor0}, {Emax1, Lor0}})
Broaden1.Print({{"file",XASfile0}})
SpectraAv = 0
for j=14, 24 do
        TempSpect = CreateSpectra(XASHamiltonian, {TXASx, TXASy, TXASz}, psiList[j], {{"Emin",Emin1}, {"Emax",Emax1}, {"NE",NE1a}})
        SpectraAv = SpectraAv + Spectra.Sum(TempSpect, {1,1,1})/3.
end
Broaden1=Spectra.Broaden(SpectraAv, Gamma0, {{Emin1, Lor0}, {Emax1, Lor0}})
Broaden1.Print({{"file",XASfile1}})
SpectraAv2 = 0
for j=25, 33 do
        TempSpect = CreateSpectra(XASHamiltonian, {TXASx, TXASy, TXASz}, psiList[j], {{"Emin",Emin1}, {"Emax",Emax1}, {"NE",NE1a}})
        SpectraAv2 = SpectraAv2 + Spectra.Sum(TempSpect, {1,1,1})/3.
end
Broaden2=Spectra.Broaden(SpectraAv2, Gamma0, {{Emin1, Lor0}, {Emax1, Lor0}})
Broaden2.Print({{"file",XASfile2}})
SpectraAv3 = 0
for j=34, 40 do
        TempSpect = CreateSpectra(XASHamiltonian, {TXASx, TXASy, TXASz}, psiList[j], {{"Emin",Emin1}, {"Emax",Emax1}, {"NE",NE1a}})
        SpectraAv3 = SpectraAv3 + Spectra.Sum(TempSpect, {1,1,1})/3.
end
Broaden3=Spectra.Broaden(SpectraAv3, Gamma0, {{Emin1, Lor0}, {Emax1, Lor0}})
Broaden3.Print({{"file",XASfile3}})
SpectraAv4 = 0
for j=41, 45 do
```

```
        TempSpect = CreateSpectra(XASHamiltonian, {TXASx, TXASy, TXASz}, psiList[j], {{"Emin",Emin1}, {"Emax",Emax1}, {"NE",NE1a}})
        SpectraAv4 = SpectraAv4 + Spectra.Sum(TempSpect, {1,1,1})/3.
end
Broaden4=Spectra.Broaden(SpectraAv4, Gamma0, {{Emin1, Lor0}, {Emax1, Lor0}})
Broaden4.Print({{"file",XASfile4}})
SpectraAv5 = 0
for j=46, 48 do
        TempSpect = CreateSpectra(XASHamiltonian, {TXASx, TXASy, TXASz}, psiList[j], {{"Emin",Emin1}, {"Emax",Emax1}, {"NE",NE1a}})
        SpectraAv5 = SpectraAv5 + Spectra.Sum(TempSpect, {1,1,1})/3.
end
Broaden5=Spectra.Broaden(SpectraAv5, Gamma0, {{Emin1, Lor0}, {Emax1, Lor0}})
Broaden5.Print({{"file",XASfile5}})
SpectraAv6 = 0
for j=49, 49 do
        TempSpect = CreateSpectra(XASHamiltonian, {TXASx, TXASy, TXASz}, psiList[j], {{"Emin",Emin1}, {"Emax",Emax1}, {"NE",NE1a}})
        SpectraAv6 = SpectraAv6 + Spectra.Sum(TempSpect, {1,1,1})/3.
end
Broaden6=Spectra.Broaden(SpectraAv6, Gamma0, {{Emin1, Lor0}, {Emax1, Lor0}})
Broaden6.Print({{"file",XASfile6}})
SpectraAv7 = 0
for j=50, 58 do
        TempSpect = CreateSpectra(XASHamiltonian, {TXASx, TXASy, TXASz}, psiList[j], {{"Emin",Emin1}, {"Emax",Emax1}, {"NE",NE1a}})
        SpectraAv7 = SpectraAv7 + Spectra.Sum(TempSpect, {1,1,1})/3.
end
Broaden7=Spectra.Broaden(SpectraAv7, Gamma0, {{Emin1, Lor0}, {Emax1, Lor0}})
Broaden7.Print({{"file",XASfile7}})
```

References

1. Lang, J.K., Baer, Y & Cox, P.A. Study of the 4f and valence band density of states in rare-earth metals: II. Experiment and results. *J. Phys. F: Met. Phys.* **11,** 121–138 (1981). https://doi.org/10.1088/0305-4608/11/1/015
2. Kaganov, M. I.,Lifshitz, I. M. & Tanatarov, L. V. Relaxation between Electrons and Crystalline Lattice. *JETP* **4**, 173 (1957).
3. Chen, J., Tzou, D. & Beraun, J. A semiclassical two-temperature model for ultrafast laser heating. *Int. J. Heat Mass Transf*. **49**, 307 (2006). https://doi.org/10.1016/j.ijheatmasstransfer.2005.06.022
4. Hill, R. W., Cosier, J., Hukin, D. A., Wells, P. & Lanchester, P. C. The specific heat of terbium below 4 K. *Phys. Lett. A* 49, 101 (1974). https://doi.org/10.1016/0375-9601(74)90689-6
5. Einstein, A. Die Plancksche Theorie der Strahlung und die Theorie der spezifischen Wärme. *Annalen der Physik* 327, 180 (1907). https://doi.org/10.1002/andp.19063270110
6. Hüttner, B. On the temperature dependence of the electronic thermal conductivity in metals when the electron and phonon subsystems are not in local equilibrium. *J. Phys.: Condens. Matter* **10**, 6121 (1998). https://doi.org/10.1088/0953-8984/11/35/313
7. Bovensiepen, U. Coherent and incoherent excitations of the Gd(0001) surface on ultrafast timescales. *J. Phys.: Condens. Matter* **19**, 083201 (2007). https://doi.org/10.1088/0953-8984/19/8/083201
8. Frietsch, B. et.al. The role of ultrafast magnon generation in the magnetization dynamics of rare-earth metals. *Science Advances* **6**, eabb1601 (2020). https://doi.org/10.1126/sciadv.abb1601
9. Thole, B. T. & van der Laan, G. Branching ratio in x-ray absorption spectroscopy. *Phys. Rev. B* 38, 3158—3171 (1988). https://link.aps.org/doi/10.1103/PhysRevB.38.3158
10. Thole, B. T., Cowan, R. D., Sawatzky, G. A., Fink, J. & Fuggle, J. C. New probe for the ground-state electronic structure of narrow-band and impurity systems. *Phys. Rev. B* **31**, 6856(R)–6858 (1985). https://doi.org/10.1103/PhysRevB.31.6856
11. Cowan, R. D. *The Theory of Atomic Structure and Spectra*. (University of California Press, 1981).
12. de Groot, F. & Kotani, A. *Core Level Spectroscopy of Solids*. (CRC Press, 2008).
13. de Groot, F. Multiplet effects in X-ray spectroscopy. *Coord. Chem. Rev.* **249**, 31–63 (2005). https://doi.org/10.1016/j.ccr.2004.03.018
14. Haverkort, M. W. Quanty for core level spectroscopy - excitons, resonances and band excitations in time and frequency domain. *J. Phys. Conf. Ser.* **712**, 012001 (2016). https://doi.org/10.1088/1742-6596/712/1/012001
15. Haverkort, M. W., Zwierzycki, M. & Andersen, O. K. Multiplet ligand-field theor using Wannier

orbitals. *Phys. Rev. B* **85**, 165113 (2012). https://doi.org/10.1103/PhysRevB.85.165113

16. Haverkort, M. W. *et al.* Bands, resonances, edge singularities and excitons in core level spectroscopy investigated within the dynamical mean-field theory. *EPL* **108**, 57004 (2014). https://doi.org/10.1209/0295-5075/108/57004
17. Lang, J. K., Baer, Y. & Cox, P. A. Study of the 4f and valence band density of states in rare-earth metals: II. Experiment and results. *J. Phys. F: Met. Phys.* **11,** 121–138 (1981). https://doi.org/10.1088/0305-4608/11/1/015
18. Weaver, J. H., Krafka, C., Lynch, D. W. & Koch, E. E. *Physik Daten- Optical Properties of metals.* pp 145 (Fachinformationszentrum Karlsruhe, 1981)
19. Frietsch, B. et.al. A high-order harmonic generation apparatus for time- and angle-resolved photoelectron spectroscopy. *Rev. Sci. Instrum.* **84**, 075106 (2013). https://doi.org/10.1063/1.4812992

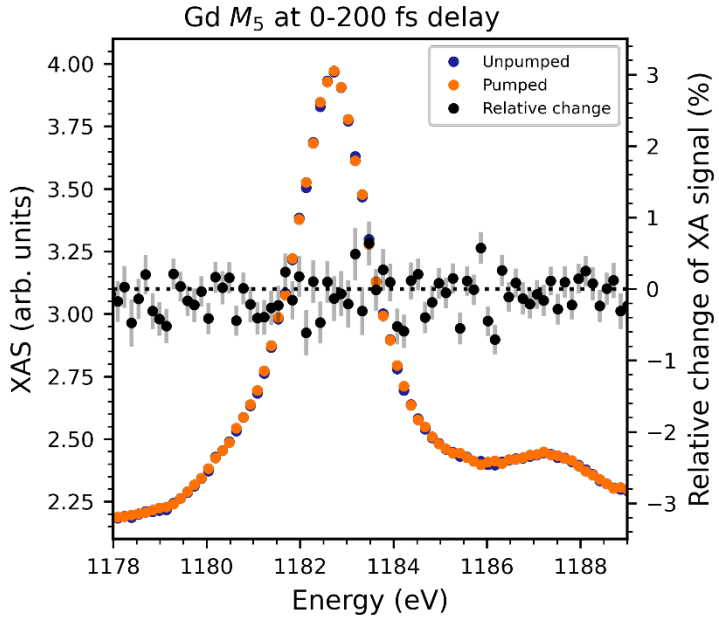

Figure S1

XA spectrum of the Gd M_5-edge averaged over an interval of 0-200 fs after excitation with an 800-nm pump pulse (orange dots) in comparison to the spectrum for the unpumped sample (blue dots), and their difference (black markers). The pump-effect is negligible, below the noise level.

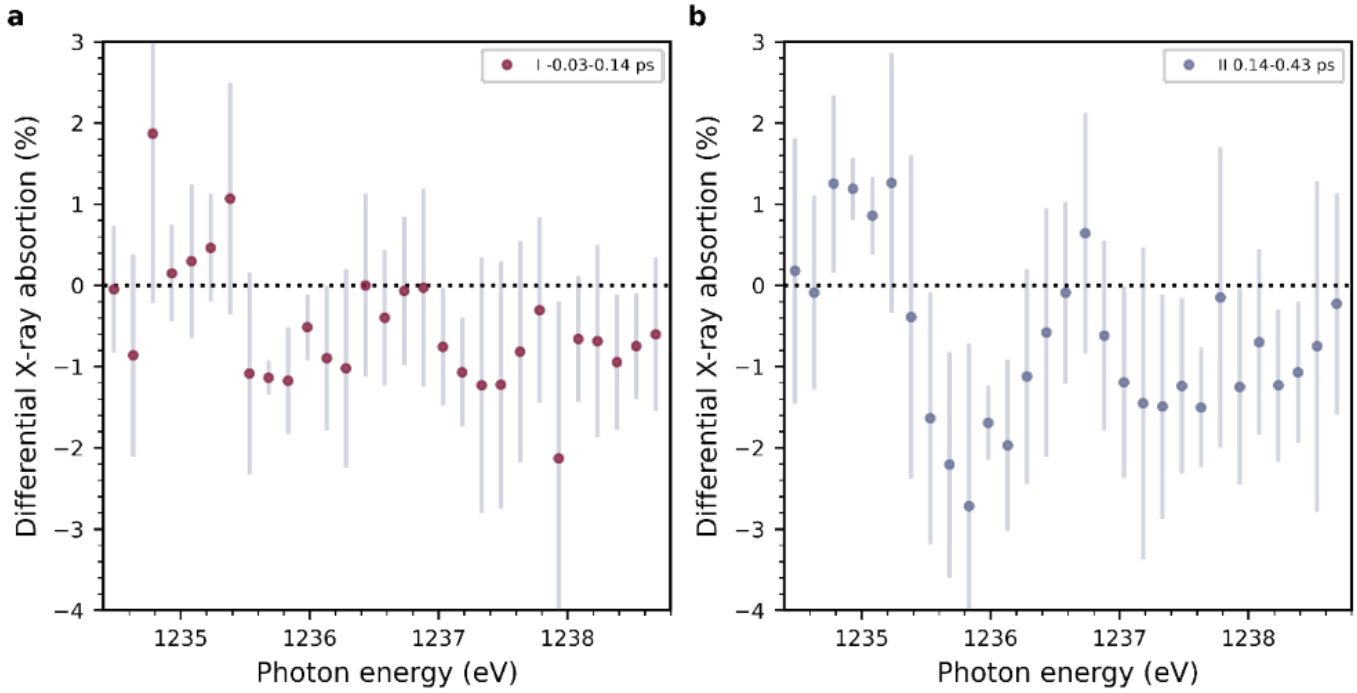

Figure S2

Differential X-ray absorption at the Tb M_5 resonance in the time intervals (I) -0.03-0.14 ps (a) and (II) 0.14-0.43 ps (b). The error bars are the error propagated standard deviation of the measured signals I_T and I_0 for the unpumped sample.

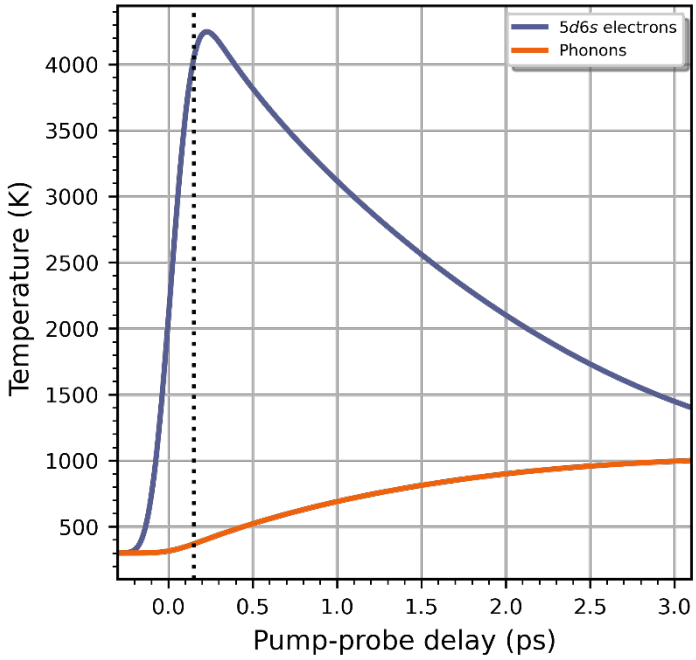

Figure S3

Dynamics of electron (blue) and lattice (orange) temperatures. The dashed vertical line indicates T_{el} ~ 4000 K reached at a pump-probe delay of 150 fs.

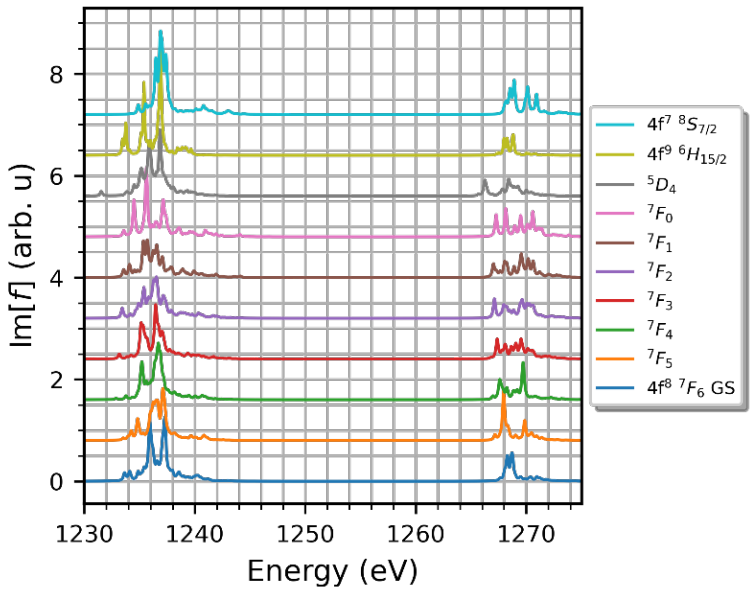

Figure S4

Calculation of multiplet transitions. The spectroscopic symbols denote the 4f configuration $^{2S+1}L_J$, where *S*, *L* and *J* are the spin, orbital and total angular momentum, respectively. In the Tb ground state $4f^8\ ^7F_6$ spins pair to $S = 3$, with orbital momentum $L = 3$ ($m_\ell = 3$) and $J = L + S = 6$. $^7F_5$ to $^7F_0$ are transitions within the singly occupied 4*f* sub-shell ($m_\ell = 2, 1, \ldots, -2$). $^5D_4$ is the first $4f^8$ spin flip transition, and $4f^7$ and $4f^9$ are multiplet excitations after 5*d*-4*f* electron transfer. Corresponding excitation energies are listed in Tab. S3.

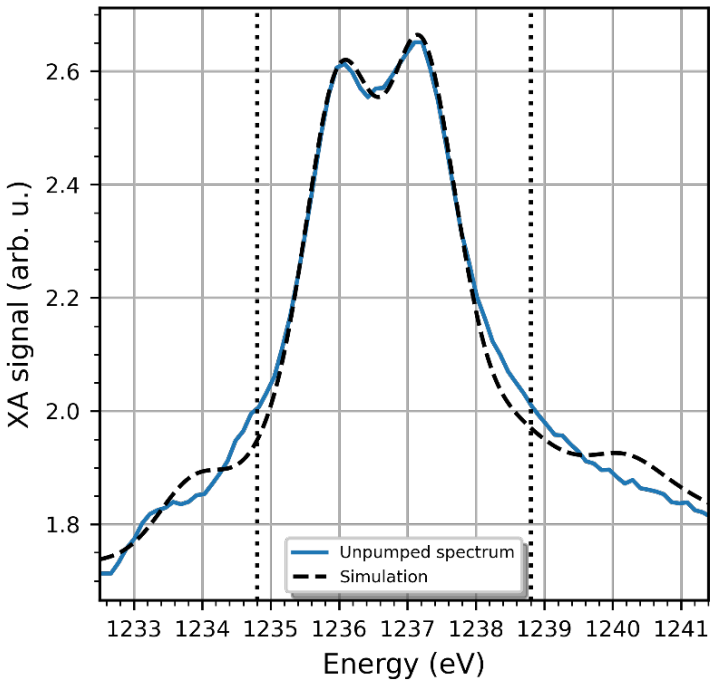

Figure S5

Simulation of the *unpumped* Tb M_5 XA spectrum with the parameters shown in Table S4. The solid line (blue) marks the experimental XA data and the dashed line (black) shows the simulation. We restrict the fit to the main two peaks in the energy range of 1234.8 to 1238.8 eV (dashed vertical lines).

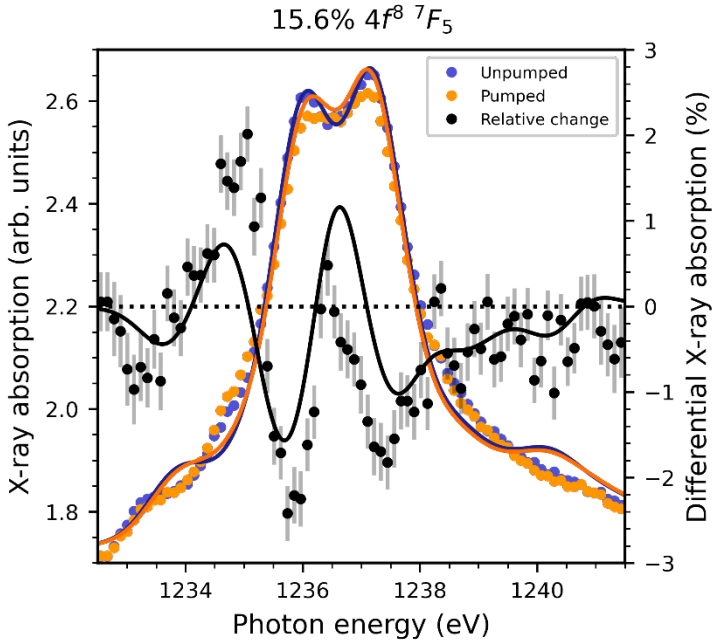

Figure S6

Tb M_5 resonance at 150 fs pump-probe delay for pumped (orange dots) and unpumped sample (blue dots), as well as the differential X-ray absorption plotted to the right abscissa (black dots). The error bars are deduced from the error propagated standard deviation of the measured transmission I_T and I_0. The lines show the simulation of the data, based on a fit of the difference signal, assuming admixtures of the lowest $^7F_5$ multiplet to the GS. We find best agreement for 15.6% $^7F_5$ and 84.4% GS contribution.

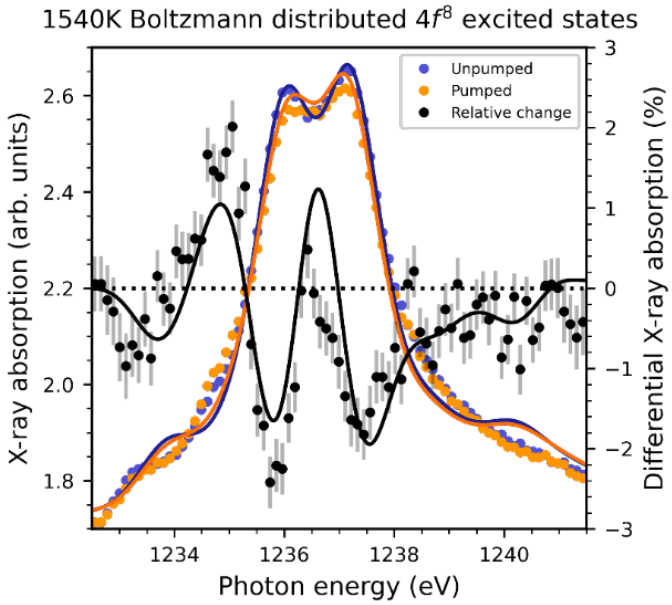

Figure S7

Tb M_5 resonance at 150 fs pump-probe delay, as well as the differential X-ray absorption (dots). The lines show the simulation of the data, based on a fit of the difference signal, assuming an admixture of Boltzmann-distributed $4f^8$ excited multiplets to the GS. We find best agreement for a Boltzmann occupation with 1540 K.

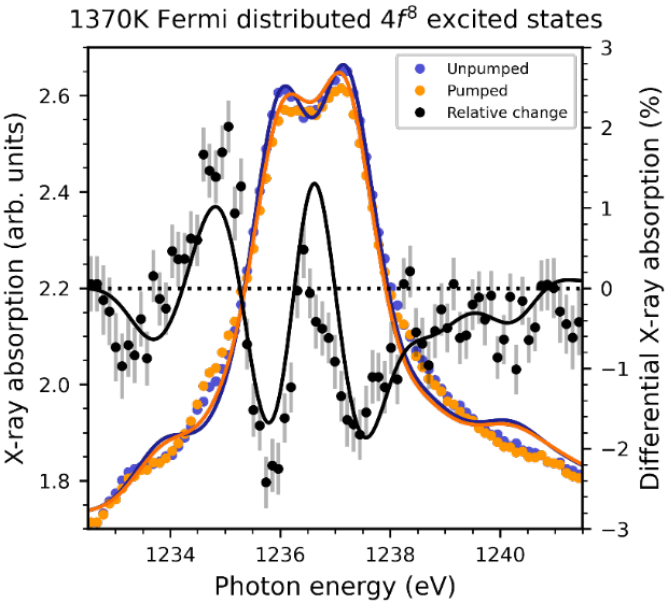

Figure S8

Tb M_5 resonance at 150 fs pump-probe delay, as well as the differential X-ray absorption (dots). The lines show the simulation of the data, based on a fit of the difference signal, assuming admixtures of $4f^8$ excited multiplets to the GS scaled with an integrated Fermi function. We find best agreement for a 1370 K Fermi profile.

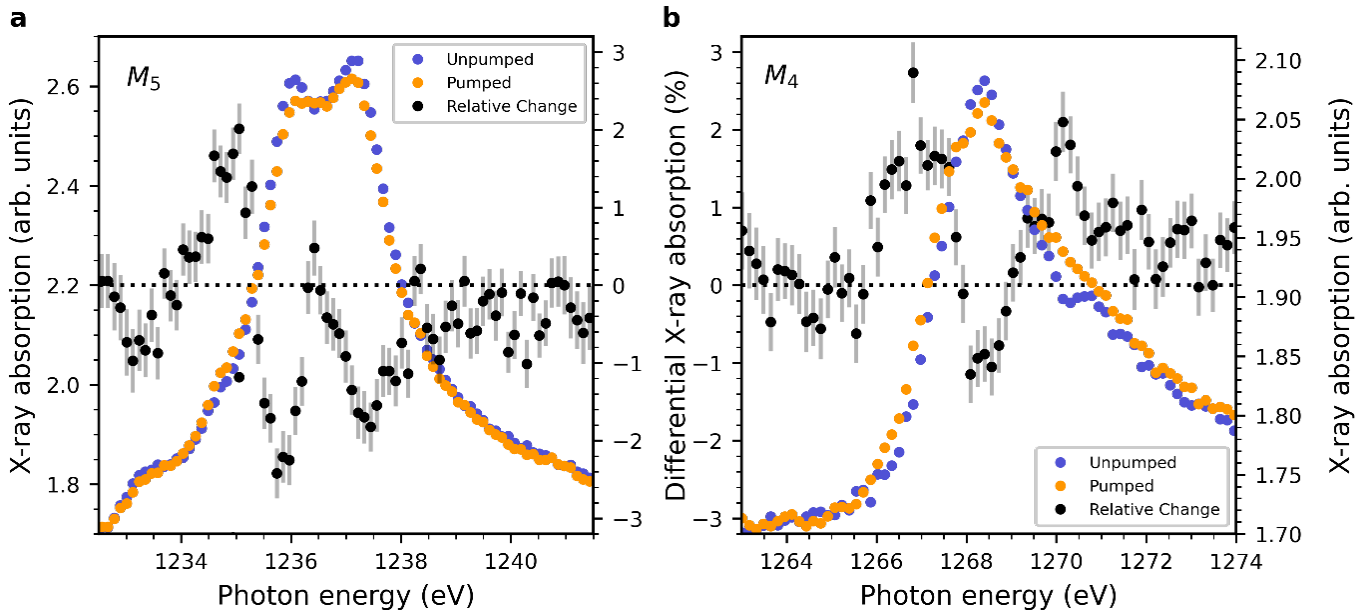

Figure S9

Tb M_5 resonance at 150 fs (**a**) and M_4 resonance at 180 fs (**b**) pump-probe delay for the pumped (orange dots) and unpumped sample (blue dots), as well as the differential absorption (black dots). The error bars denote the error propagated standard deviation of the measured signals I_T and I_0. While the integrated XA signal at the M_5 edge decreases upon pumping, the signal at the M_4 edge increases.